Deep learning-enhanced design for functionally graded auxetic lattices

Jinghui Li[a] , Deepak Kumar Pokkalla[b], Zhen-Pei Wang[c*] , Yingjun Wang[a*]

[a]*National Engineering Research Center of Novel Equipment for Polymer Processing, the Key Laboratory of Polymer Processing Engineering of the Ministry of Education (South China University of Technology), Guangdong Provincial Key Laboratory of Technique and Equipment for Macromolecular Advanced Manufacturing, South China University of Technology, Guangzhou, 510641, China*

[b]*Manufacturing Science Division, Oak Ridge National Laboratory, Oak Ridge, TN 37932, USA*

[c]*Institute of High Performance Computing (IHPC), Agency for Science, Technology and Research (A*STAR), 1 Fusionopolis Way, 138632, Singapore.*

Abstract

Auxetic materials with counterintuitive negative Poisson's ratio have been of significant interest due to potential applications across diverse engineering fields. Functionally grading such auxetics further enables customization of the structural response and harnesses the potential for multi-functional applications. However, a critical challenge in designing functionally graded lattices is to efficiently determine

---

[*] Corresponding author
Email address: wangzp@ihpc.a-star.edu.sg (Zhen-Pei Wang)
[*] Corresponding author
Email address: wangyj84@scut.edu.cn (Yingjun Wang)

the spatial variation of the functional gradient and the corresponding geometric designs to achieve the desired response. In this paper, a highly efficient deep learning-based inverse design framework for functionally graded tetra-petal auxetics with spatially tailored properties is presented. This framework significantly improves the efficiency of tailoring functionally graded auxetics where many unit cells need to be tailor-designed. The graded tetra-petal auxetics obtained from the inverse design framework are additively manufactured and subjected to impact tests. The results show superior impact performance compared with uniform designs, demonstrating the effectiveness of the proposed inverse design framework, which can be inspirable to promote advanced structures/materials with enhanced impact resistance.

Keywords Functionally Graded Lattices, Deep Learning, Inverse Design, Auxetics, Additive Manufacturing, Impact Test

1. Introduction

Functionally graded materials (FGMs) are a type of materials that comprise a spatial gradation in local geometry, density, and/or composition customized for a specific performance or function [1], which can be found widely in nature, such as bamboo, bones, and tree trunks. The gradation in such materials offers a great design space for tailoring the structural and functional performance while satisfying other considerations such as light weighting. FGMs have been of increased interest in recent years due to their wide use in aerospace applications [2, 3], sensors [4, 5], biomaterial [6-8], electronics [9, 10], energy absorption [11, 12]. With the use of readily available modelling software like nTopology [13], Altair [14] or Materialise [15], and recent advancements in additive manufacturing (AM) techniques, modeling and fabrication of graded lattices is becoming increasingly feasible. The focus of this paper is to propose a deep learning-based inverse design strategy for rapidly identifying functionally graded auxetic lattices.

Auxetic materials contracting transversely under an axial compression load exhibit a negative Poisson’s ratio (NPR) phenomenon. Due to this NPR effect, auxetics exhibit enhanced mechanical properties such as indentation or shear resistance [16, 17], energy absorption [18-20], and wave propagation characteristics [21]. Auxetics can be found in nature, for example, α-cristobalite [22] and crystalline SiO2 [23] as well as human-designed, namely, star-shaped structure[24], re-entrant structure [25-27], chiral structure [21, 28, 29], rotating triangles structure [30], rotating squares structure[31], petal-shaped structure[32-34], and missing rib structures[35, 36]. Spatially grading auxetic unit cells within a macrostructure could enable improvements in properties as it leverages both the functional grading and NPR effects. To this end, functionally graded auxetic materials made up of double arrowhead honeycomb [37], inverted tetrapods [38], and reentrant honeycomb [39] under impact have been studied. The weak Young’s modulus and strength are indeed a problem for typical cellular/lattice materials and structures. Studies of using novel metamaterial forms with enhanced mechanical properties are important in critical applications, e.g., using graphene origami-enabled metamaterials to achieve enhanced mechanical properties [40-43].

Despite the promise of improved mechanical properties by combining auxetic and spatial grading effects, functionally graded auxetic structures aren’t fully explored. Here, a functional grading of tetra-petal auxetics with improved impact properties is proposed. FGMs based on tetra-petal unit cells have two advantages: First, the properties of tetra-petal unit cells can be tuned over a wide range, thus enabling functionally graded tetra-petals with multiple gradient properties. Second, the unit cells of graded tetra-petals can be seamlessly connected to adjacent ones with connecting bars. Spatially integrating such unit cells that offer tunable mechanical properties locally enables achieving improved mechanical responses at the macroscale. This is investigated in this paper through the design and additive manufacturing of uniform and graded auxetic structures.

The geometry features of auxetic unit cells can be described by identifying key parameters such as lengths and angles, and the effective elastic properties of unit cells can be obtained through numerical simulations or experiments [29-33]. Most of the existing studies for designing structural components, particularly lattices or auxetics, are based on iterative numerical simulations or expensive experimentation. However, rapidly predicting the auxetic design with prescribed mechanical responses is crucial for critical applications i.e., an inverse search of auxetic geometric design for a given mechanical property. Several gradient-based and heuristic design optimization approaches have been investigated in the literature. Based on a genetic algorithm and finite element method, Javadi et al. generated a larger bunch of auxetic materials with a wide range of negative Poisson’s ratios[44]. Clausen et al. used topology optimization to design auxetic structures with prescribed Poisson’s ratios [45]. Integrating isogeometric analysis with shape optimization in linear [32, 33] and nonlinear [46] regimes, petal auxetics with prescribed elastic and nonlinear properties were designed. Using genetic algorithm, a class of four- and six-ligament missing rib auxetics were designed over large strains [35, 36]. Moreover, several researchers designed auxetics with tunable effective properties [33, 47]. Liao et al. achieved tetra-chiral auxetics inverse design through deep learning [48]. Wang et al. presented an approach to rapidly predict elastic properties of petal auxetics using back-propagation neural networks (BPNN) and tested the design limits of tri-petal and hexa-petal auxetics via inverse design[49]. These recent studies illustrate the potential of neural network-based inverse design strategy for rapidly identifying auxetics with target mechanical properties and form the basis for the current work.

Several researchers have investigated functionally graded auxetic designs in the literature. Hou et al. spliced hexagonal structure and re-entrant structure to a graded one [50]. Hou et al. changed the height of auxetic cellular structures in graded layers [51]. Xiao et al. varied reentrant honeycomb cell-wall thickness to construct graded structure [39]. Qi et al. construct graded hybrid-chiral and anti-chiral structures by diversifying the ligament size [52]. The aforementioned works focus on investigating the gradual variation of geometric parameters and their impact on mechanical properties. However, the mechanical properties of graded auxetic lattices do not change in the same way as the graded geometric variation. Hence, it's more effective to determine the mechanical properties variation within the auxetic lattice structure and rapidly design the auxetic unit cells matching desired effective properties at corresponding locations.

Fabricating functionally graded auxetic lattices with traditional processing methods is challenging due to their complex geometries. The need to ensure high geometrical accuracy to achieve the desired functional performance poses a critical challenge for their fabrication using traditional methods. Additive manufacturing (AM) provides the capability to create structures with composition, microstructural, and porosity gradients [53] due to its intrinsic layer-by-layer printing nature and paves the way for fabricated graded lattice structures. Surface-based graded lattice structures with gradual variation in density and unit cell size have been fabricated using AM and tested experimentally[54, 55]. Functionally graded auxetics based on 3D-lattice [56] and re-entrant [57] unit cells were also fabricated using AM and tested mechanically. Thus, AM is chosen for fabricating functionally graded auxetic lattices in this study.

In this paper, a deep neural network (DNN)-based strategy for rapid inverse design of tetra-petal auxetic lattice is proposed. The DNN-based method is highly efficient and enables rapid spatial tailoring of geometries with desirable local properties. The efficiency of the proposed framework is demonstrated through the design of some tetra-petal unit cells. The auxetic designs obtained were fabricated using AM and the effective mechanical properties are evaluated through impact tests.

The potential of this strategy for designing functionally graded tetra-petal auxetic structures with improvements in energy absorption is shown.

The paper is organized as follows: In Section 2, a deep learning-based inverse design framework for tetra-petal auxetics is presented. In Section 3, the generation of uniform and functionally graded tetra-petal auxetic lattices along with their fabrication procedure is entailed. Section 4 describes the impact test and compares the impact performance of graded tetra-petal auxetic lattices with uniform lattices. The conclusion is presented in Section 5.

2. Deep learning-based inverse design of tetra-petal auxetics

2.1 Inverse design of tetra-petal unit cells

Petal-shaped auxetics that contain three to six petals are obtained by smoothening the sharp vertices of the traditional star-shaped auxetic structures. Smoothening the vertices alleviated the stress concentration effect and significantly improved the auxetic performance [32, 46]. For instance, the tetra-petal auxetics consisting of four petals and four connecting bars as shown in Fig. 1a exhibits a large range of tunable auxeticity and effective stiffness [34]. Particularly, the effective performance is dominated by the petal geometry and changing the bar size does not affect the effective properties significantly (refer Fig. 1f [34]). This makes tetra-petal auxetics a good choice for functional grading as the unit cells can be stacked or connected through the bars alleviating the issues arising from incompatibility in hierarchical or heterogeneous architected materials.

In this work, functionally graded tetra-petal auxetic lattices with hierarchical units are designed by setting all the unit cells with a side length of 20 mm (Fig. 1b) and the connecting bar sizes of unit cells in the same auxetic lattice are identical. Thus, the design domain of each unit cell is a squared region with a dimension of $20\text{mm} \times 20\text{mm}$. To preserve the curved features and control the number of design variables, a NURBS-based design parametrization with only 8 design parameters (Fig. 1 c-e) is used [33]. NURBS-based isogeometric analysis seamlessly integrates the curved geometrical description of the petals, and the corresponding FE analysis is employed for the numerical analysis [32, 33].

A typical inverse design framework for tetra-petal unit cells is depicted in Fig. 2a [33]. Given target effective properties, gradient-based iterative optimization is performed to find a tetra-petal unit cell geometry with desired effective properties. The mathematical expressions of the optimization algorithm are listed as follows:

$$\begin{aligned} & min \quad \varphi(\boldsymbol{\alpha}) = (\bar{v} - \tilde{\bar{v}})^2 \\ & s.t. \\ & \qquad \phi(\boldsymbol{\alpha}) = \bar{E} - \tilde{\bar{E}} = 0 \\ & \qquad \underline{\mathbf{x}_\mathrm{i}} \leq \boldsymbol{\alpha}_\mathrm{i} \leq \overline{\mathbf{x}_\mathrm{i}}, \ \mathrm{i}=1,2,\cdots,8 \end{aligned} \tag{1}$$

where $\boldsymbol{\alpha}$ is the set of design parameters ([a1, a3, a4, a5, h5, c1, c2, c3] that are illustrated in Fig. 1 c-e) that characterize the geometry of unit cells; $\bar{v}$ is the effective Poisson's ratio; $\tilde{\bar{v}}$ is the target effective Poisson's ratio; $\bar{E}$ is the effective Young's modulus; $\tilde{\tilde{E}}$ is the target effective Young’s modulus; $\underline{\mathbf{x}_\mathrm{i}}$ and $\overline{\mathbf{x}_\mathrm{i}}$ are the lower and upper bound of design parameter $\boldsymbol{\alpha}_\mathrm{i}$, given by $\underline{\mathbf{x}_\mathrm{i}}$ = [0.8, 0.35, 0.5, 0.25, 7, 0.3, 0.2, 0.2] $\overline{\mathbf{x}_\mathrm{i}}$ = [3, 3, 3, 1, 13.5, 1, 1, 1.5].

2.2 Deep Neural Network-based inverse design strategy

In a standard approach, the effective properties of numerous designs during the iterative optimization process are evaluated using the computational homogenization method (Fig. 2a). Such an iterative approach deems to be computationally expensive if many unit cells need to be designed for a large-scale heterogenous lattice structure. To this end, a back-propagation neural network (BPNN) that serves as a surrogate model is proposed to significantly improve the design efficiency for the following superiorities:

- Compared with the computational homogenization approach, the BPNN can predict the effective properties almost instantaneously, which reduces computing time significantly.
- Design sensitivity analysis based on computational homogenization is complicated and the accuracy may be affected by the perturbation rate if a non-analytical method is used, while for the BPNN, the sensitivity analysis can be concisely, quickly, and easily calculated using an explicit analytical function.

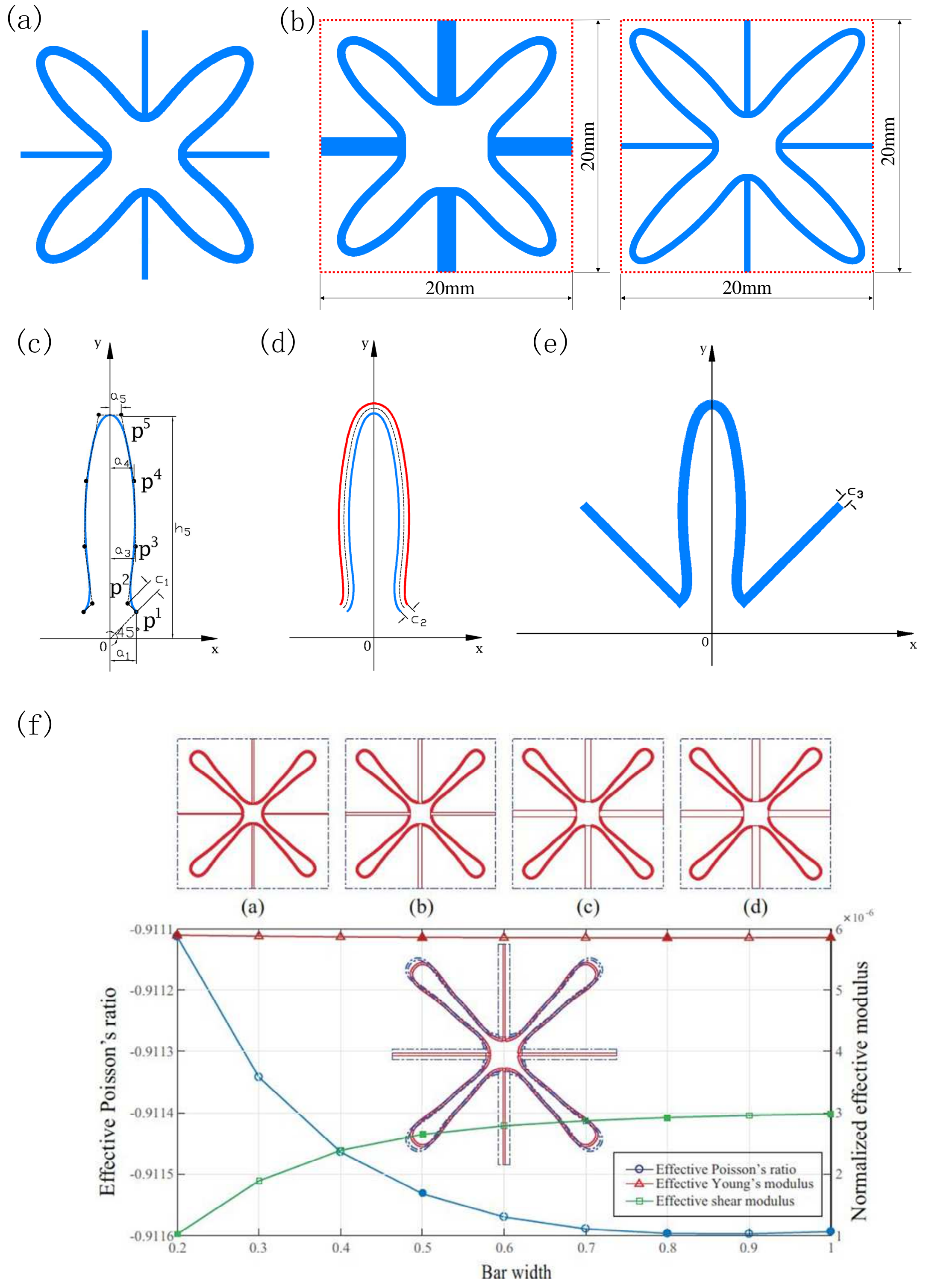

Figure 1. (a)Tetra-petal unit cell. (b) Outer size of tetra-petal unit cells. (c) The inner boundary of a tetra-petal unit cell and its dimension definition. (d) The inner and outer boundary of a tetra-petal unit cell. (e) Connecting bars' generation and width. (f) Influence of bar width on effective elastic properties [34].

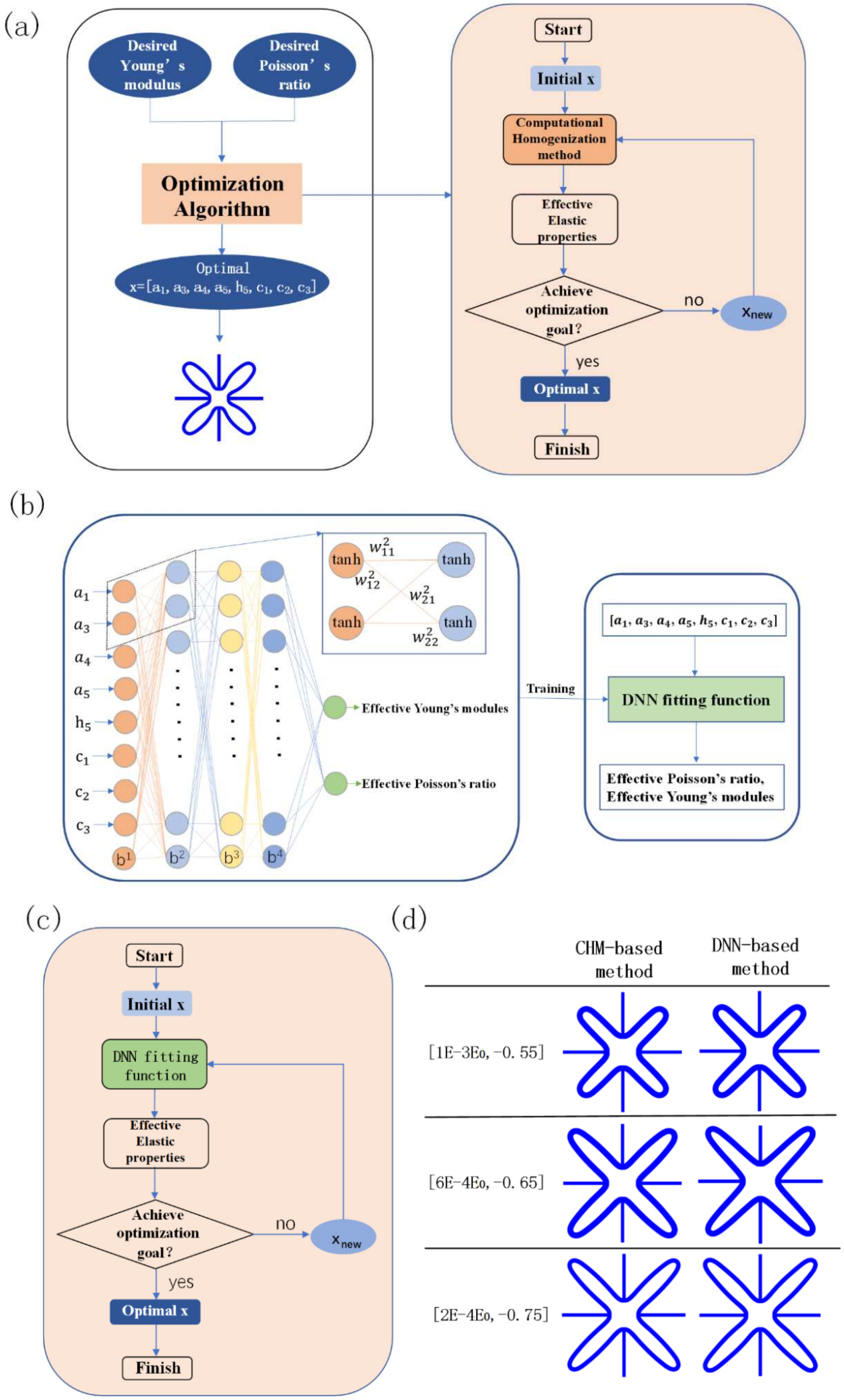

Figure 2. (a) Optimization method of tetra-petal unit cell design based on

computational homogenization method. (b) DNN structure. (c) Optimization method of tetra-petal unit cell design based on DNN fitting function. (d) Three tetra-petal unit cells generated using optimization methods based on the computational homogenization method (left) and the DNN approach.

Training a BPNN in the present context is a regression that establishes a mapping between the geometric design parameters as inputs and the effective properties as outputs. To ensure the accuracy of the surrogate model, a deep neural network (DNN) with two or more hidden layers can be utilized. The current framework consists of an input layer with eight neurons corresponding to 8 input design parameters that describe tetra-petal geometry, three hidden layers, and one output layer with two neurons predicting the effective Poisson's ratio and Young's modulus, as shown in Fig. 2b. The DNN can be used to replace the computational homogenization method for predicting effective properties for a new design parametrization during the inverse design of tetra-petal auxetics (Fig. 2c). A detailed account of such a DNN can be found in the work of Liao et. al. [48]. The DNN datasets of the training, validation, and test are 8050, 3450, and 500, respectively. The relative error (absolute value) distributions of the two effective property indexes for the test set are plotted in Fig 3. The relative error of the effective Poisson's ratios for some samples is large because the actual effective Poisson's ratio is close to zero.

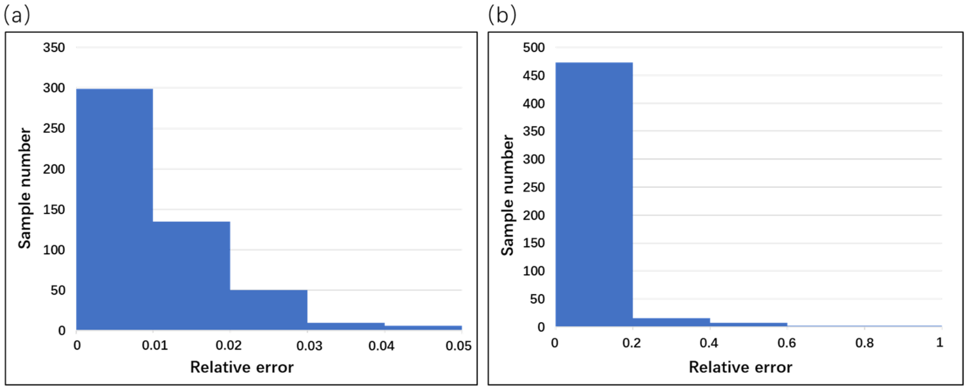

Figure 3. (a) The relative error (absolute value) distribution of the effective Young's modulus. (b) The relative error (absolute value) distribution of the effective Poisson's ratio.

Next, three tetra-petal design cases with different target properties were considered to compare the computational efficiency of the design optimization using computational homogenization and DNN-based approaches. The target Young's modulus and Poisson's ratio for the three cases are set as [1E-3E_0, -0.55], [6E-4E_0, -0.65], and [2E-4E_0, -0.75], respectively, where E_0 is the base material Young's modulus. The designed tetra-petals are shown in Fig. 2d. The accuracy and performance of these design approaches are compared in Table 1. The DNN-based approach significantly reduced the design optimization cost as compared to the computational homogenization-based approach.

Table 1 Comparison of computational homogenization-based and DNN-based methods.

	CHM-based method			DNN-based method		
	Time	Effective	Effective	Time [s]	Effective	Effective

	[s]	Young's modulus	Poisson's ratio		Young's modulus	Poisson's ratio
[1E-3E_0, -0.55]	773.60	1.00E-3 E_0	-0.55	7.92	1.00E-3 E_0	-0.56
[6E-4E_0, -0.65]	532.67	6.00E-4 E_0	-0.65	4.81	5.98E-4 E_0	-0.66
[2E-4E_0, -0.75]	573.05	2.00E-4 E_0	-0.75	4.89	1.97E-4 E_0	-0.76

3. Design and fabrication of functionally graded tetra-petal auxetic lattices

3.1 DNN-enhanced design framework for functionally graded tetra-petal auxetic lattices

Functionally graded lattices can be designed to provide a trade-off between structural and functional performance while ensuring light-weighting. In this study, the impact performance of functionally graded tetra-petal auxetics is investigated. To design such lattices, unit cells at different locations need to be tailored individually or in groups and the inverse design of each unit cell can be costly using traditional computational homogenization-based approach. Here, a lattice structure with three layers of grading with the same tetra-petal design throughout a given layer is adopted. A DNN-based inverse design approach is utilized for rapidly designing the graded auxetic lattices. The design domain of the lattice structure is a rectangular region with a dimension of $60\text{mm} \times 62\text{mm}$, with the top and bottom layer having a thickness of 1mm.

Lattice structures with overall dimensions of $60\text{mm} \times 62\text{mm}$ are inversely designed using the DNN-based design optimization approach. First, two graded auxetic lattices were obtained with effective Poisson’s ratios of -0.7 and -0.5, respectively. The three graded layers are designed to have an effective Young’s moduli of approximately 1.0E-04 E_0, 3.0E-04 E_0 and 9.0E-04 E_0, respectively. Next, three standard uniform lattices are obtained with an effective Poisson’s ratio of -0.7 and different effective Young’s moduli of approximately 1.0E-04 E_0, 3.0E-04 E_0 and 9.0E-04 E_0. The actual elastic properties of the tetra-petal auxetic unit cells calculated by the computational homogenization approach are summarized in Table 2. The geometries of tetra-petal unit cells are shown in Fig. 4d.

Table 2 The actual elastic properties of the designed tetra-petal unit cells calculated by the computational homogenization method.

	Effective Young’s modulus	Effective Poisson’s ratio
U7_1	1.01E-04 E_0	-0.691
U7_3	3.00E-04 E_0	-0.694
U7_9_1	8.94E-04 E_0	-0.719
U7_9_2	8.93E-04 E_0	-0.703
U5_1	1.02E-04 E_0	-0.491
U5_3	3.03E-04 E_0	-0.493
U5_9	8.99E-04 E_0	-0.495

Inversely designed tetra-petal unit cells and the construction of all the digital models were performed with a desktop computer, Y900 341SZ, with a CPU of the Intel(R) Core (TM) i7-6700K CPU @ 4.00GHz. The RAM is 16GB. The GPU is

NVIDIA GeForce GTX 1080. All uniform and graded tetra-petal digital models are constructed using Rhino 6. Two thin plates were added to the top and bottom of the lattice models for stabilizing the lattice surface during the impact tests, as shown in Fig. 4b.

The graded lattices can be oriented in two different ways during the impact testing, either the softer layer to be placed upwards or downwards. In this study, a graded auxetic lattice structure with the Poisson's ratio of -0.7 and an increasing or decreasing stiffness is labelled as 7_139 or 7_931, respectively (refer Fig. 4a). Similarly, the graded lattice structure with a Poisson's ratio of -0.5 is labelled as 5_139 or 5_931 depending upon the soft layer placed either upward or downward, respectively (refer Fig. 4a). The uniform auxetic lattices with different effective Young's modulus of 1.0E-04 E_0, 3.0E-04 E_0 and 9.0E-04 E_0 are referred as 7_111, 7_333, and 7_999_1 (refer Fig.4c), hereinafter. It should be noted that all three lattice structures with uniform cells have the same-sized thin connecting bars, and inevitably, the stability under impact decreases significantly as the unit stiffness increases. To ensure stability, an extra auxetic lattice for the petal unit with larger-sized connecting bars but the same moduli of 9.0E-04 E_0 is fabricated, termed 7_999_2 hereinafter, and the corresponding unit cell is termed U7_9_2.

3.2 **Additive manufacturing of auxetic lattices**

The generated uniform and graded auxetic lattice structures with a thickness of

60mm were fabricated with Flexible 80A resin in a Form 2 3D printer (Formlabs Inc., Boston USA) using stereolithography. The material properties of the resin are listed in Table 3. The geometric models were sliced using PreForm 3.23.1 software. All printed samples were washed in ethanol 75% (Fu Yu Fine Chemicals Ltd. - Tianjin, China) to remove residual liquid resin and cured under the sun light before the support removal. The 3D-printed tetra-petal auxetic structures are illustrated in Fig. 4e.

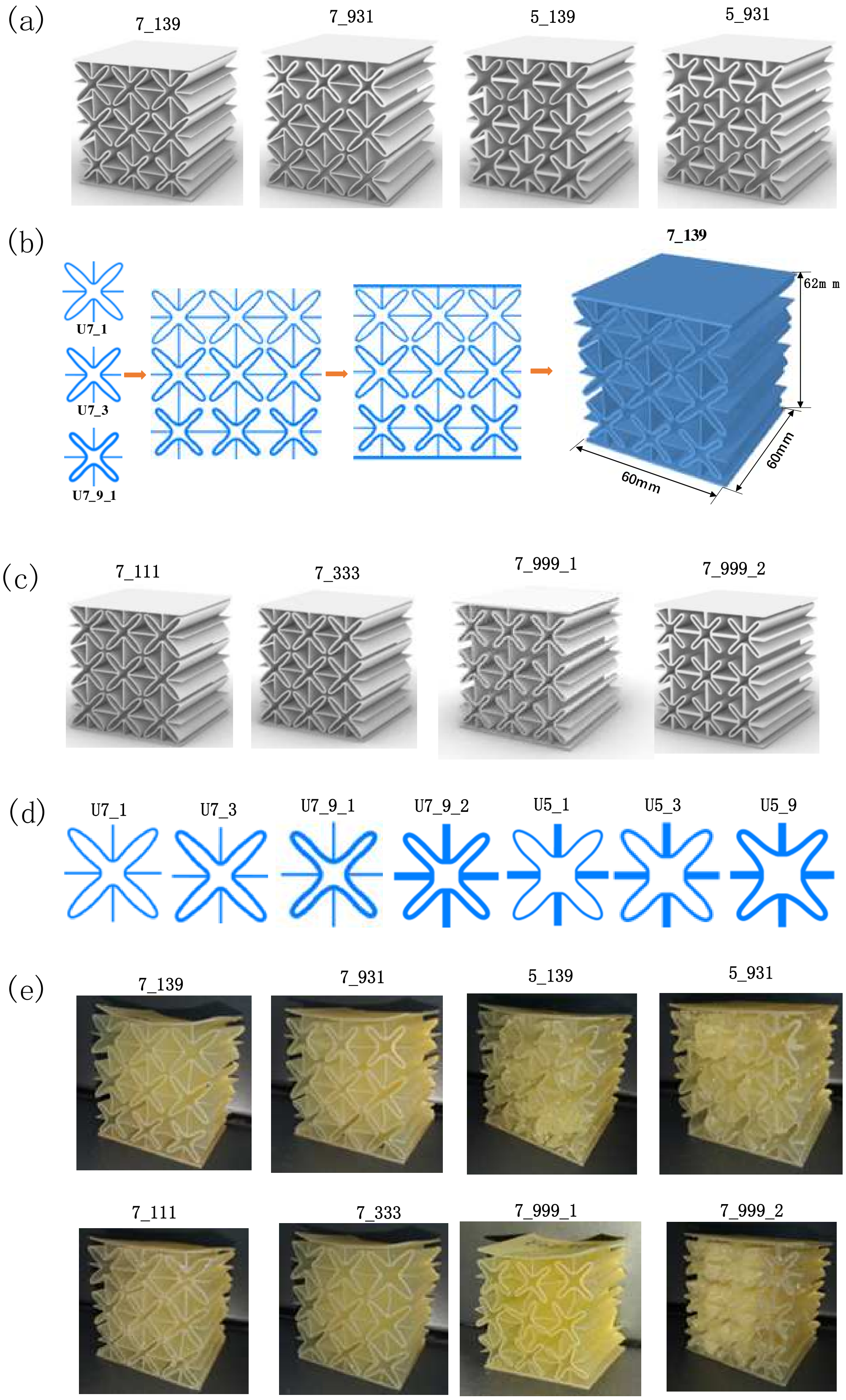

Figure 4. (a) Four graded auxetic lattices. (b) Model construction process. (c) Four non-graded auxetic lattices. (d) Tetra-petal unit cells. (e) 3D- printed samples. The

first number, 7, in U7_1, U7_3…, and 7_139,7_931 represents the unit cells with an effective Poisson's ratio of approximately -0.7. The second number in U7_1, U7_3…, represents the relative Young's modulus. For example, U7_1 represents the unit cell with an effective Poisson's ratio of approximately -0.7 and a Young's modulus of approximately 1.0E-04E$_0$, while U7_3 represents the unit cell with an effective Poisson's ratio of approximately -0.7 and a Young's modulus of approximately 3.0E-04E$_0$. The numbers after the underscore in 7_139,7_931… denote the construction of the auxetic lattice setting. For example, 7_139 represents the auxetic lattice formed by unit cells of U7_1 in the top layer, U7_3 in the middle layer, and U7_9 in the bottom layer, respectively; while U7_931 means the auxetic lattice formed by unit cells of U7_9 in the top layer, U7_3 in the middle layer, and U7_9 in the bottom layer, respectively.

Table 3 Resin material properties[58].

	Green	Post-cured
Ultimate tensile strength	3.7 MPa	8.9 MPa
Stress at 50% Elongation	1.5 MPa	3.1 MPa
Stress at 100% Elongation	3.5 MPa	6.3 MPa
Elongation at Break	100%	120%
Tear Strength	11 kN/m	24 kN/m

4. Impact tests of functionally graded tetra-petal auxetic lattices

4.1 Impact test setting

Impact tests are performed on the functionally graded auxetic lattice samples by placing them on a platform as shown in Fig. 5a. The platform consists of a support column, a support arm, a hollow cylindrical guide rail, a height adjuster, an impact pedestal, and an impact rod. Before commencing experiments, the hollow cylindrical guide rail is set to be vertical with ground to make sure that the impact rod falls smoothly, and the friction effect is minimized. The samples are aligned along the hollow cylindrical guide rail such that the impact rod falls on the centers of the samples. In a test, the impact rod is lifted to a certain level and released so that it falls onto the samples and the reaction force is measured by an acceleration sensor (Fig. 5b) simultaneously. To ensure the measurement precision and protect the sensor from damage during the test, the acceleration sensor is glued to a dice firmly and the assembly and disassembly of the impact rod are acted on the dice rather than directly on the sensor (Fig. 5c). The arrow engraved on the sensor represents its positive direction. The measured acceleration is negative when it is pointing upward.

4.2 Results

Impact tests for all samples are performed with the impact rod released from 5cm, 10cm, and 15cm above the top of the samples (Fig. 5d). To ensure that sensor collects the whole impact process data, the impact rod is released after the sensor is triggered. Each impact test is repeated five times to reduce the experimental error. The acceleration sensor outputs acceleration-time graphs and the peak acceleration magnitudes are recorded. For each tetra-petal sample, the datasets from five experimental repetitions with the same release height are acquired. The datasets with the minimum and the maximum peak acceleration speed are removed, and the rest three data sets are retained, as depicted in Table 4. The averages of all peak acceleration rates are compared in Fig. 6. It should be noted that the maximum acceleration magnitudes of the uniform sample 7_999_2 at 15cm are out of the acceleration sensor range (± 490 $\mathrm{m/s^2}$)[59] and hence the data collected for this testing case are not reliable, which is marked with underlines.

Table 4 Three retained maximum acceleration magnitudes and the averages of these quantities for all test samples at three different rod-releasing heights.

	5cm				10cm				15cm			
	Three maximum acceleration magnitudes [$\mathrm{m/s^2}$]			AVG [$\mathrm{m/s^2}$]	Three maximum acceleration magnitudes [$\mathrm{m/s^2}$]			AVG [$\mathrm{m/s^2}$]	Three maximum acceleration magnitudes [$\mathrm{m/s^2}$]			AVG [$\mathrm{m/s^2}$]
7_111	111.15	112.20	112.52	111.96	171.43	172.67	174.27	172.79	209.66	210.85	215.33	211.95
7_333	115.45	116.96	117.60	116.67	194.41	198.17	201.97	198.18	240.42	242.43	251.22	244.69
7_999_2	288.99	289.22	292.83	290.35	478.23	481.70	483.31	481.08	604.02	609.60	610.75	608.12
7_139	95.86	99.38	99.88	98.37	143.51	146.12	150.05	146.56	182.51	190.02	194.14	188.89
7_931	104.64	106.06	106.89	105.86	153.49	156.23	162.78	157.5	185.81	195.05	204.12	194.99
5_139	123.18	124.05	127.94	125.06	183.33	188.69	188.83	186.95	260.15	269.81	272.69	267.55
5_931	122.18	124.28	124.88	123.78	184.02	184.48	186.26	184.92	253.83	254.15	255.62	254.53

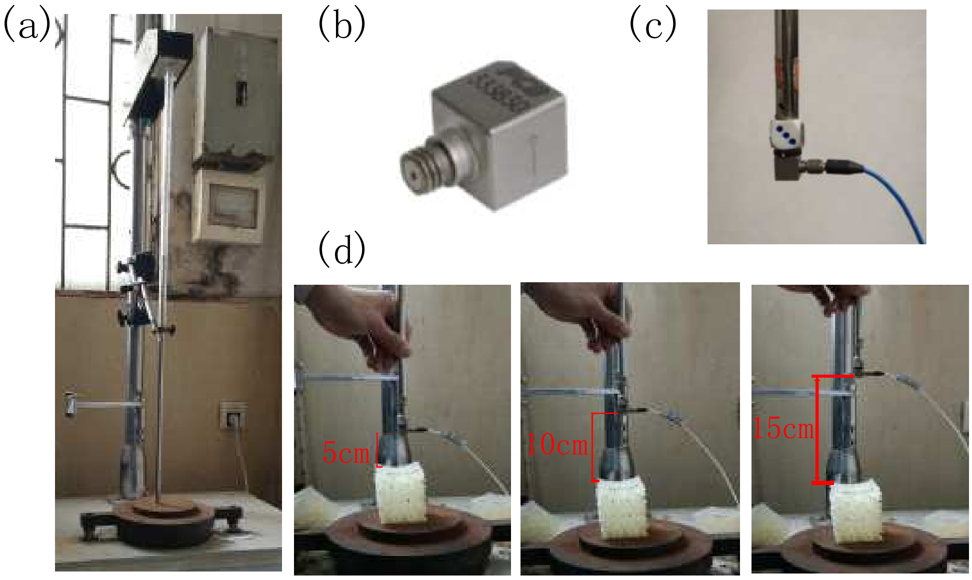

Figure 5. (a) Impact test platform. (b) Acceleration sensor. (c) Attachment of the acceleration sensor and the impact rod. (d) The impact rod is released from a height of 5cm, 10cm, and 15cm, respectively.

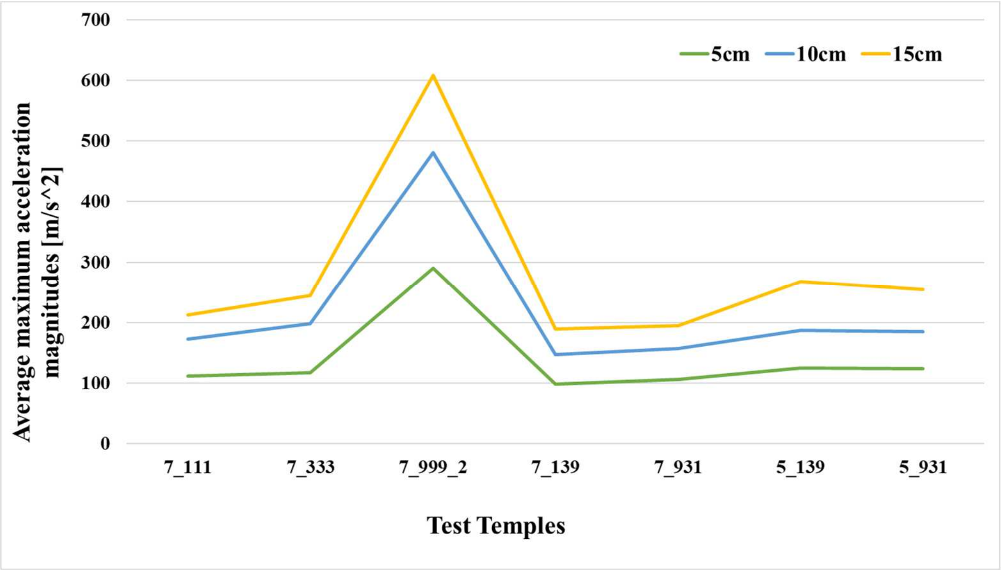

Figure 6. The average maximum acceleration magnitudes of all test samples with different levels of impact energy.

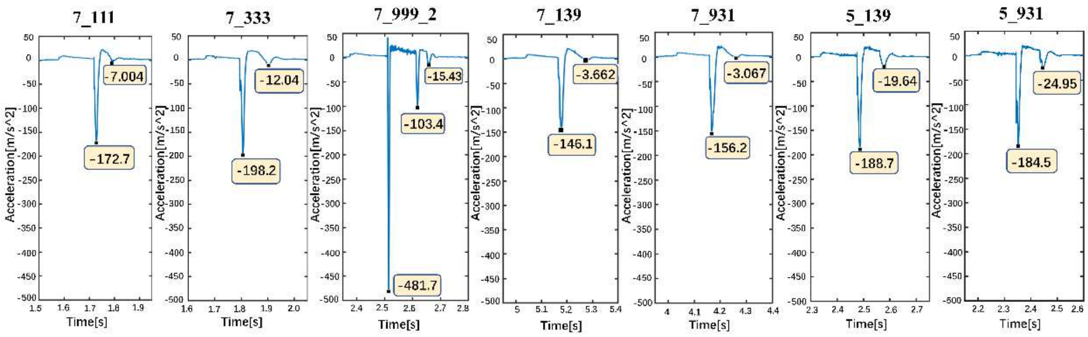

Figure 7. Acceleration curves of all test samples for the cases where the impact rod is released at a height of 10cm.

As shown in Fig 6, for every tetra-petal sample, the higher the impact energy is, the larger the average peak acceleration rate is. The differences between the average maximum acceleration magnitudes of samples 7_139 and 7_931 are 7.61% at 5cm, 7.46% at 10cm, and 3.23% at 15cm. Lattice sample 7_139 performs better than sample 7_931 for all three impact settings. Compared with sample 7_111 with uniform cells U7_1, graded sample 7_931 reduces the maximum acceleration magnitude by 5.45% at 5cm, 8.85% at 10cm, and 8.00% at 15cm. Compared with sample 7_333 with uniform cells U7_3, graded sample 7_931 reduces the average maximum acceleration magnitudes by 9.27% at 5cm, 20.53% at 10cm, and 20.31% at 15cm. Compared with sample 7_999_2 with uniform cells U7_9_2, graded sample 7_931 reduces the average maximum acceleration magnitudes by 63.54% at 5cm, 67.26% at 10cm, and 67.94% at 15cm. In summary, graded samples 7_139 and 7_931 perform better than uniform cell samples 7_111, 7_333, and 7_999_2. The differences between the average maximum acceleration magnitudes of graded samples 5_139 and 5_931 are -1.02% at 5cm, -1.09% at 10cm, and -4.87% at 15cm. Graded sample

5_931 has a slightly better performance at all three impact heights than sample 5_931. Compared with sample 5_931, sample 7_931 reduces the average maximum acceleration magnitudes by 14.48% at 5cm, 14.83% at 10cm, and 23.39% at 15cm. Graded samples 7_139 and 7_931 reduce the maximum acceleration magnitude more significantly than samples 5_139 and 5_931, indicating graded tetra-petals auxetic lattices with a Poisson's ratio of -0.7 have better performance than those with a Poisson's ratio of -0.5.

Selected acceleration-time graphs with a rod dropping height of 10 cm are depicted in Fig. 7. As shown in the graphs, all acceleration graphs show almost the same change trend along the time axis. The peak acceleration rates are negative, indicating that the resistance load from the samples to the impact rod is pointing upward. All graphs have only two upward acceleration peak values and the second peak value is prominently smaller than the first one, except the uniform sample 7_999_2 which has three peak values. For all cases, the second acceleration peak values reduce by 95.94% (uniform sample 7_111), 93.93% (uniform sample 7_333), 78.53% (uniform sample 7_999_2), 97.49% (graded sample 7_139), 98.04% (graded sample 7_931), 89.59% (graded sample 5_139), and 86.48% (graded sample 5_931), respectively, compared with the first acceleration peak values. This indicates that the impact rod does not have any obvious bounce after contacting with the samples.

5. Conclusion

The DNN trained to map the relation between geometry parameters of tetra-petal units and their effective elastic properties significantly improves the inverse design efficiency, compared with the traditional design approach using computational homogenization. This is favorable for functionally graded lattices where inverse tailor design is required locally for many unit cells. Leveraging such an efficient inverse design framework using DNN, we propose to design functionally graded tetra-petal auxetic lattices using the DNN-based inverse approach, with remarkable effectiveness and efficiency. Additive manufacturing technology is utilized to prototype the functionally graded and non-graded samples. Impact tests are performed over different designs and the results show promising performances. The improved impact resistance of graded auxetic lattice structures proves the feasibility of the proposed inverse design framework for functionally graded tetra-petal auxetic, which can be inspirable and helpful to promote advanced functional materials and structures with tunable behaviors.

Appendix

Table A1 The geometric parameters of tetra-petal unit cells.

Tetra-petals	α							
U7_1	1.41	1.37	1.28	0.60	11.95	0.66	0.54	0.50
U7_3	1.36	1.24	0.96	0.61	11.72	0.64	0.77	0.50
U7_9_1	1.27	0.39	0.70	0.45	10.05	0.70	0.96	0.50

U7_9_2	1.11	0.62	0.70	0.46	9.34	0.73	0.92	1.50
U5_1	1.86	1.56	1.59	0.62	10.61	0.64	0.48	1.50
U5_3	1.77	1.36	1.39	0.62	10.12	0.66	0.67	1.50
U5_9	2.00	0.96	0.85	0.48	9.97	0.53	0.94	1.50

Acknowledgements

This work is supported by National Natural Science Foundation of China [No. 52075184] (J. Li, Y. Wang). This research is supported by A*STAR <C210112026> (Z. P. Wang). Portions of the research were supported by the U.S. Department of Energy, Office of Energy Efficiency and Renewable Energy, Industrial Technologies Program, under contract DE-AC05–00OR22725 with UT Battelle, LLC.

References

[1] Wessel JK. The handbook of advanced materials: enabling new designs: John Wiley & Sons; 2004.

[2] Nemat-Alla M. Reduction of thermal stresses by developing two-dimensional functionally graded materials. International journal of solids and structures. 2003;40:7339-56.

[3] Choi KH, Kim H-S, Park CH, Kim G-H, Baik KH, Lee SH et al. High-temperature thermo-mechanical behavior of functionally graded materials produced by plasma sprayed coating: Experimental and modeling results. Metals and Materials International. 2016;22:817-24.

[4] Bahrami S, Ovesy HR, Shakeri M. Dynamic analysis of functionally graded circular cylindrical panel with piezoelectric fiber composite actuator and sensor. Journal of Intelligent Material Systems and Structures. 2015;26:2369-85.

[5] Atashipour S, Sburlati R. Electro-elastic analysis of a coated spherical piezoceramic sensor. Composite Structures. 2016;156:399-409.

[6] Mehrali M, Shirazi FS, Mehrali M, Metselaar HSC, Kadri NAB, Osman NAA. Dental implants from functionally graded materials. Journal of Biomedical Materials Research Part A: An Official Journal of The Society for Biomaterials, The Japanese Society for Biomaterials, and The Australian Society for Biomaterials and the Korean Society for Biomaterials. 2013;101:3046-57.

[7] Lowen JM, Leach JK. Functionally graded biomaterials for use as model systems and replacement tissues. Advanced Functional Materials. 2020;30:1909089.
[8] Zhu C, Qiu J, Thomopoulos S, Xia Y. Augmenting Tendon‐to‐Bone Repair with Functionally Graded Scaffolds. Advanced Healthcare Materials. 2021;10:2002269.
[9] Zhang Y, Malyi OI, Tang Y, Wei J, Zhu Z, Xia H et al. Reducing the charge carrier transport barrier in functionally layer‐graded electrodes. Angewandte Chemie. 2017;129:15043-8.
[10] Rasel S, Bhatkar O, Smith D, Kowal MD, Anderson M, Rizvi R et al. Self-assembled functionally graded graphene films with tunable compositions and their applications in transient electronics and actuation. ACS applied materials & interfaces. 2019;11:23463-73.
[11] Xu F, Zhang X, Zhang H. A review on functionally graded structures and materials for energy absorption. Engineering Structures. 2018;171:309-25.
[12] Baroutaji A, Arjunan A, Stanford M, Robinson J, Olabi AG. Deformation and energy absorption of additively manufactured functionally graded thickness thin-walled circular tubes under lateral crushing. Engineering Structures. 2021;226:111324.
[13] NTopology. Architected Materials. [cited 2023 January 8th]; Available from: https://ntopology.com/architected-materials/.
[14] Altair. Altair OptiStruct® Revolutionizes Lattice Structures for 3D Printing. [cited 2023 January 8th]; Available from: http://www.altairhyperworks.com/newsdetail.aspx?news_id=11109&news_country=en-US
[15] Materialise. Materialise 3-matic Lightweight Structures Module. [cited 2023 January 8th]; Available from: http://www.materialise.com/en/software/3-matic/modules/lightweight-structures-module
[16] Dirrenberger J, Forest S, Jeulin D. Effective elastic properties of auxetic microstructures: anisotropy and structural applications. International Journal of Mechanics and Materials in Design. 2013;9:21-33.
[17] Alderson KL, Fitzgerald A, Evans KE. The strain dependent indentation resilience of auxetic microporous polyethylene. Journal of Materials Science. 2000;35:4039-47.
[18] Zhu Y, Wang Z-P, Poh LH. Auxetic hexachiral structures with wavy ligaments for large elasto-plastic deformation. Smart Materials and Structures. 2018;27:055001.
[19] Zhu Y, Zeng Z, Wang Z-P, Poh LH, Shao Y. Hierarchical hexachiral auxetics for large elasto-plastic deformation. Materials Research Express. 2019;6:085701.
[20] Zhao X, Wei L, Wen D, Zhu G, Yu Q, Ma Z. Bending response and energy absorption of sandwich beams with novel auxetic honeycomb core. Engineering Structures. 2021;247:113204.
[21] Spadoni A, Ruzzene M, Gonella S, Scarpa F. Phononic properties of hexagonal chiral lattices. Wave motion. 2009;46:435-50.
[22] Yeganeh-Haeri A, Weidner DJ, Parise JB. Elasticity of α-cristobalite: a silicon dioxide with a negative Poisson's ratio. Science. 1992;257:650-2.
[23] Keskar NR, Chelikowsky JR. Negative Poisson ratios in crystalline SiO2 from first-principles calculations. Nature. 1992;358:222-4.

[24] Theocaris P, Stavroulakis G, Panagiotopoulos P. Negative Poisson's ratios in composites with star-shaped inclusions: a numerical homogenization approach. Archive of Applied Mechanics. 1997;67:274-86.

[25] Masters I, Evans K. Models for the elastic deformation of honeycombs. Composite structures. 1996;35:403-22.

[26] Smith CW, Grima J, Evans K. A novel mechanism for generating auxetic behaviour in reticulated foams: missing rib foam model. Acta materialia. 2000;48:4349-56.

[27] Zhu Y, Luo Y, Gao D, Yu C, Ren X, Zhang C. In-plane elastic properties of a novel re-entrant auxetic honeycomb with zigzag inclined ligaments. Engineering Structures. 2022;268:114788.

[28] Prall D, Lakes R. Properties of a chiral honeycomb with a Poisson's ratio of—1. International Journal of Mechanical Sciences. 1997;39:305-14.

[29] Spadoni A, Ruzzene M. Elasto-static micropolar behavior of a chiral auxetic lattice. Journal of the Mechanics and Physics of Solids. 2012;60:156-71.

[30] Grima JN, Evans KE. Auxetic behavior from rotating triangles. Journal of materials science. 2006;41:3193-6.

[31] Grima JN, Evans KE. Auxetic behavior from rotating squares. Journal of Materials Science Letters. 2000;19:1563-5.

[32] Wang Z-P, Poh LH, Dirrenberger J, Zhu Y, Forest S. Isogeometric shape optimization of smoothed petal auxetic structures via computational periodic homogenization. Computer Methods in Applied Mechanics and Engineering. 2017;323:250-71.

[33] Wang Z-P, Poh LH. Optimal form and size characterization of planar isotropic petal-shaped auxetics with tunable effective properties using IGA. Composite Structures. 2018;201:486-502.

[34] Wang Z-P, Poh LH, Zhu Y, Dirrenberger J, Forest S. Systematic design of tetra-petals auxetic structures with stiffness constraint. Materials & Design. 2019;170:107669.

[35] Pokkalla DK, Poh LH, Quek ST. Isogeometric shape optimization of missing rib auxetics with prescribed negative Poisson' s ratio over large strains using genetic algorithm. International Journal of Mechanical Sciences. 2021;193:106169.

[36] Pokkalla DK, Wang Z, Teoh JC, Poh LH, Lim CT, Quek ST. Soft Missing Rib Structures with Controllable Negative Poisson' s Ratios over Large Strains via Isogeometric Design Optimization. Journal of Engineering Mechanics. 2022;148:04022063.

[37] Qiao J, Chen C. Impact resistance of uniform and functionally graded auxetic double arrowhead honeycombs. International Journal of Impact Engineering. 2015;83:47-58.

[38] Novak N, Borovinšek M, Vesenjak M, Wormser M, Körner C, Tanaka S et al. Crushing behavior of graded auxetic structures built from inverted tetrapods under impact. physica status solidi (b). 2019;256:1800040.

[39] Xiao D, Dong Z, Li Y, Wu W, Fang D. Compression behavior of the graded metallic auxetic reentrant honeycomb: Experiment and finite element analysis. Materials Science and Engineering: A. 2019;758:163-71.

[40] Zhao S, Zhang Y, Wu H, Zhang Y, Yang J, Kitipornchai S. Tunable nonlinear bending behaviors of functionally graded graphene origami enabled auxetic metamaterial beams. Composite Structures. 2022;301:116222.

[41] Zhao S, Zhang Y, Zhang Y, Yang J, Kitipornchai S. Vibrational characteristics of functionally graded graphene origami-enabled auxetic metamaterial beams based on machine learning assisted models. Aerospace Science and Technology. 2022;130:107906.

[42] Zhao S, Zhang Y, Wu H, Zhang Y, Yang J. Functionally graded graphene origami-enabled auxetic metamaterial beams with tunable buckling and postbuckling resistance. Engineering Structures. 2022;268:114763.

[43] Zhao S, Zhang Y, Zhang Y, Yang J, Kitipornchai S. A functionally graded auxetic metamaterial beam with tunable nonlinear free vibration characteristics via graphene origami. Thin-Walled Structures. 2022;181:109997.

[44] Akbar, A., Javadi, Asaad, Faramarzi, Raziyeh et al. Design and optimization of microstructure of auxetic materials. Engineering Computations. 2012;29:260-76.

[45] Clausen A, Wang F, Jensen JS, Sigmund O, Lewis JA. Topology optimized architectures with programmable Poisson’ s ratio over large deformations. Adv Mater. 2015;27:5523-7.

[46] Pokkalla DK, Wang Z-P, Poh LH, Quek ST. Isogeometric shape optimization of smoothed petal auxetics with prescribed nonlinear deformation. Computer Methods in Applied Mechanics and Engineering. 2019;356:16-43.

[47] Zhu Y, Jiang S, Li J, Pokkalla DK, Wang Q, Zhang C. Novel isotropic anti-tri-missing rib auxetics with prescribed in-plane mechanical properties over large deformations. International Journal of Applied Mechanics. 2021;13:2150115.

[48] Liao Z, Wang Y, Gao L, Wang Z-P. Deep-learning-based isogeometric inverse design for tetra-chiral auxetics. Composite Structures. 2022;280:114808.

[49] Wang Y, Liao Z, Shi S, Wang Z, Poh LH. Data-Driven Structural Design Optimization for Petal-Shaped Auxetics Using Isogeometric Analysis. Computer Modeling in Engineering & Sciences. 2020:122.

[50] Hou Y, Neville R, Scarpa F, Remillat C, Gu B, Ruzzene M. Graded conventional-auxetic Kirigami sandwich structures: Flatwise compression and edgewise loading. Composites Part B: Engineering. 2014;59:33-42.

[51] Hou W, Yang X, Zhang W, Xia Y. Design of energy-dissipating structure with functionally graded auxetic cellular material. International Journal of Crashworthiness. 2018;23:366-76.

[52] Qi D, Lu Q, He C, Li Y, Wu W, Xiao D. Impact energy absorption of functionally graded chiral honeycomb structures. Extreme Mechanics Letters. 2019;32:100568.

[53] Mahmoud D, Elbestawi MA. Lattice structures and functionally graded materials applications in additive manufacturing of orthopedic implants: a review. Journal of Manufacturing and Materials Processing. 2017;1:13.

[54] Maskery I, Aremu AO, Parry L, Wildman RD, Tuck CJ, Ashcroft IA. Effective design and simulation of surface-based lattice structures featuring volume fraction and cell type grading. Materials & Design. 2018;155:220-32.

[55] Plocher J, Panesar A. Effect of density and unit cell size grading on the stiffness and energy absorption of short fibre-reinforced functionally graded

lattice structures. Additive Manufacturing. 2020;33:101171.
[56] Li C, Shen H-S, Wang H. Nonlinear dynamic response of sandwich plates with functionally graded auxetic 3D lattice core. Nonlinear Dynamics. 2020;100:3235-52.
[57] Wu X, Su Y, Shi J. In-plane impact resistance enhancement with a graded cell-wall angle design for auxetic metamaterials. Composite Structures. 2020;247:112451.
[58] Formlabs. RESIN FAMILY-Flexible and Elastic. [cited 2022 May 13]; Available from: https://formlabs.com/materials/flexible-elastic/.
[59] PCB. Model : 333B30 | Accelerometer, ICP®. [cited 2022 May 13]; Available from: https://www.pcb.com/products?m=333b30.

Deep learning-enhanced design for functionally graded auxetic lattices

Jinghui Li[a] , Deepak Kumar Pokkalla[b], Zhen-Pei Wang[c*] , Yingjun Wang[a*]

[a]*National Engineering Research Center of Novel Equipment for Polymer Processing, the Key Laboratory of Polymer Processing Engineering of the Ministry of Education (South China University of Technology), Guangdong Provincial Key Laboratory of Technique and Equipment for Macromolecular Advanced Manufacturing, South China University of Technology, Guangzhou, 510641, China*

[b]*Manufacturing Science Division, Oak Ridge National Laboratory, Oak Ridge, TN 37932, USA*

[c]*Institute of High Performance Computing (IHPC), Agency for Science, Technology and Research (A*STAR), 1 Fusionopolis Way, 138632, Singapore.*

Abstract

Auxetic materials with counterintuitive negative Poisson's ratio have been of significant interest due to potential applications across diverse engineering fields. Functionally grading such auxetics further enables customization of the structural response and harnesses the potential for multi-functional applications. However, a critical challenge in designing functionally graded lattices is to efficiently determine

---

[*] Corresponding author
Email address: wangzp@ihpc.a-star.edu.sg (Zhen-Pei Wang)

[*] Corresponding author
Email address: wangyj84@scut.edu.cn (Yingjun Wang)

the spatial variation of the functional gradient and the corresponding geometric designs to achieve the desired response. In this paper, a highly efficient deep learning-based inverse design framework for functionally graded tetra-petal auxetics with spatially tailored properties is presented. This framework significantly improves the efficiency of tailoring functionally graded auxetics where many unit cells need to be tailor-designed. The graded tetra-petal auxetics obtained from the inverse design framework are additively manufactured and subjected to impact tests. The results show superior impact performance compared with uniform designs, demonstrating the effectiveness of the proposed inverse design framework, which can be inspirable to promote advanced structures/materials with enhanced impact resistance.

Keywords Functionally Graded Lattices, Deep Learning, Inverse Design, Auxetics, Additive Manufacturing, Impact Test

1. Introduction

Functionally graded materials (FGMs) are a type of materials that comprise a spatial gradation in local geometry, density, and/or composition customized for a specific performance or function [1], which can be found widely in nature, such as bamboo, bones, and tree trunks. The gradation in such materials offers a great design space for tailoring the structural and functional performance while satisfying other considerations such as light weighting. FGMs have been of increased interest in recent years due to their wide use in aerospace applications [2, 3], sensors [4, 5], biomaterial [6-8], electronics [9, 10], energy absorption [11, 12]. With the use of readily available modelling software like nTopology [13], Altair [14] or Materialise [15], and recent advancements in additive manufacturing (AM) techniques, modeling and fabrication of graded lattices is becoming increasingly feasible. The focus of this paper is to propose a deep learning-based inverse design strategy for rapidly identifying functionally graded auxetic lattices.

Auxetic materials contracting transversely under an axial compression load exhibit a negative Poisson’s ratio (NPR) phenomenon. Due to this NPR effect, auxetics exhibit enhanced mechanical properties such as indentation or shear resistance [16, 17], energy absorption [18-20], and wave propagation characteristics [21]. Auxetics can be found in nature, for example, α-cristobalite [22] and crystalline SiO2 [23] as well as human-designed, namely, star-shaped structure[24], re-entrant structure [25-27], chiral structure [21, 28, 29], rotating triangles structure [30], rotating squares structure[31], petal-shaped structure[32-34], and missing rib structures[35, 36]. Spatially grading auxetic unit cells within a macrostructure could enable improvements in properties as it leverages both the functional grading and NPR effects. To this end, functionally graded auxetic materials made up of double arrowhead honeycomb [37], inverted tetrapods [38], and reentrant honeycomb [39] under impact have been studied. The weak Young’s modulus and strength are indeed a problem for typical cellular/lattice materials and structures. Studies of using novel metamaterial forms with enhanced mechanical properties are important in critical applications, e.g., using graphene origami-enabled metamaterials to achieve enhanced mechanical properties [40-43].

Despite the promise of improved mechanical properties by combining auxetic and spatial grading effects, functionally graded auxetic structures aren’t fully explored. Here, a functional grading of tetra-petal auxetics with improved impact properties is proposed. FGMs based on tetra-petal unit cells have two advantages: First, the properties of tetra-petal unit cells can be tuned over a wide range, thus enabling functionally graded tetra-petals with multiple gradient properties. Second, the unit cells of graded tetra-petals can be seamlessly connected to adjacent ones with connecting bars. Spatially integrating such unit cells that offer tunable mechanical properties locally enables achieving improved mechanical responses at the macroscale. This is investigated in this paper through the design and additive manufacturing of uniform and graded auxetic structures.

The geometry features of auxetic unit cells can be described by identifying key parameters such as lengths and angles, and the effective elastic properties of unit cells can be obtained through numerical simulations or experiments [29-33]. Most of the existing studies for designing structural components, particularly lattices or auxetics, are based on iterative numerical simulations or expensive experimentation. However, rapidly predicting the auxetic design with prescribed mechanical responses is crucial for critical applications i.e., an inverse search of auxetic geometric design for a given mechanical property. Several gradient-based and heuristic design optimization approaches have been investigated in the literature. Based on a genetic algorithm and finite element method, Javadi et al. generated a larger bunch of auxetic materials with a wide range of negative Poisson’s ratios[44]. Clausen et al. used topology optimization to design auxetic structures with prescribed Poisson’s ratios [45]. Integrating isogeometric analysis with shape optimization in linear [32, 33] and nonlinear [46] regimes, petal auxetics with prescribed elastic and nonlinear properties were designed. Using genetic algorithm, a class of four- and six-ligament missing rib auxetics were designed over large strains [35, 36]. Moreover, several researchers designed auxetics with tunable effective properties [33, 47]. Liao et al. achieved tetra-chiral auxetics inverse design through deep learning [48]. Wang et al. presented an approach to rapidly predict elastic properties of petal auxetics using back-propagation neural networks (BPNN) and tested the design limits of tri-petal and hexa-petal auxetics via inverse design[49]. These recent studies illustrate the potential of neural network-based inverse design strategy for rapidly identifying auxetics with target mechanical properties and form the basis for the current work.

Several researchers have investigated functionally graded auxetic designs in the literature. Hou et al. spliced hexagonal structure and re-entrant structure to a graded one [50]. Hou et al. changed the height of auxetic cellular structures in graded layers [51]. Xiao et al. varied reentrant honeycomb cell-wall thickness to construct graded structure [39]. Qi et al. construct graded hybrid-chiral and anti-chiral structures by diversifying the ligament size [52]. The aforementioned works focus on investigating the gradual variation of geometric parameters and their impact on mechanical properties. However, the mechanical properties of graded auxetic lattices do not change in the same way as the graded geometric variation. Hence, it's more effective to determine the mechanical properties variation within the auxetic lattice structure and rapidly design the auxetic unit cells matching desired effective properties at corresponding locations.

Fabricating functionally graded auxetic lattices with traditional processing methods is challenging due to their complex geometries. The need to ensure high geometrical accuracy to achieve the desired functional performance poses a critical challenge for their fabrication using traditional methods. Additive manufacturing (AM) provides the capability to create structures with composition, microstructural, and porosity gradients [53] due to its intrinsic layer-by-layer printing nature and paves the way for fabricated graded lattice structures. Surface-based graded lattice structures with gradual variation in density and unit cell size have been fabricated using AM and tested experimentally[54, 55]. Functionally graded auxetics based on 3D-lattice [56] and re-entrant [57] unit cells were also fabricated using AM and tested mechanically. Thus, AM is chosen for fabricating functionally graded auxetic lattices in this study.

In this paper, a deep neural network (DNN)-based strategy for rapid inverse design of tetra-petal auxetic lattice is proposed. The DNN-based method is highly efficient and enables rapid spatial tailoring of geometries with desirable local properties. The efficiency of the proposed framework is demonstrated through the design of some tetra-petal unit cells. The auxetic designs obtained were fabricated using AM and the effective mechanical properties are evaluated through impact tests.

The potential of this strategy for designing functionally graded tetra-petal auxetic structures with improvements in energy absorption is shown.

The paper is organized as follows: In Section 2, a deep learning-based inverse design framework for tetra-petal auxetics is presented. In Section 3, the generation of uniform and functionally graded tetra-petal auxetic lattices along with their fabrication procedure is entailed. Section 4 describes the impact test and compares the impact performance of graded tetra-petal auxetic lattices with uniform lattices. The conclusion is presented in Section 5.

2. Deep learning-based inverse design of tetra-petal auxetics

2.1 Inverse design of tetra-petal unit cells

Petal-shaped auxetics that contain three to six petals are obtained by smoothening the sharp vertices of the traditional star-shaped auxetic structures. Smoothening the vertices alleviated the stress concentration effect and significantly improved the auxetic performance [32, 46]. For instance, the tetra-petal auxetics consisting of four petals and four connecting bars as shown in Fig. 1a exhibits a large range of tunable auxeticity and effective stiffness [34]. Particularly, the effective performance is dominated by the petal geometry and changing the bar size does not affect the effective properties significantly (refer Fig. 1f [34]). This makes tetra-petal auxetics a good choice for functional grading as the unit cells can be stacked or connected through the bars alleviating the issues arising from incompatibility in hierarchical or heterogeneous architected materials.

In this work, functionally graded tetra-petal auxetic lattices with hierarchical units are designed by setting all the unit cells with a side length of 20 mm (Fig. 1b) and the connecting bar sizes of unit cells in the same auxetic lattice are identical. Thus, the design domain of each unit cell is a squared region with a dimension of $20\text{mm} \times 20\text{mm}$. To preserve the curved features and control the number of design variables, a NURBS-based design parametrization with only 8 design parameters (Fig. 1 c-e) is used [33]. NURBS-based isogeometric analysis seamlessly integrates the curved geometrical description of the petals, and the corresponding FE analysis is employed for the numerical analysis [32, 33].

A typical inverse design framework for tetra-petal unit cells is depicted in Fig. 2a [33]. Given target effective properties, gradient-based iterative optimization is performed to find a tetra-petal unit cell geometry with desired effective properties. The mathematical expressions of the optimization algorithm are listed as follows:

$$
\begin{aligned}
& min \quad \varphi(\boldsymbol{\alpha}) = (\bar{v} - \tilde{\bar{v}})^2 \\
& s.t. \\
& \qquad \phi(\boldsymbol{\alpha}) = \bar{E} - \tilde{\bar{E}} = 0 \\
& \qquad \underline{\mathbf{x}_{\mathrm{i}}} \le \boldsymbol{\alpha}_{\mathrm{i}} \le \overline{\mathbf{x}_{\mathrm{i}}}, \ \mathrm{i}=1,2,\cdots,8
\end{aligned}
\tag{1}
$$

where $\boldsymbol{\alpha}$ is the set of design parameters ([a1, a3, a4, a5, h5, c1, c2, c3] that are illustrated in Fig. 1 c-e) that characterize the geometry of unit cells; $\bar{v}$ is the effective Poisson's ratio; $\tilde{\bar{v}}$ is the target effective Poisson's ratio; $\bar{E}$ is the effective Young's modulus; $\tilde{\tilde{E}}$ is the target effective Young's modulus; $\underline{\mathbf{x}_\mathrm{i}}$ and $\overline{\mathbf{x}_\mathrm{i}}$ are the lower and upper bound of design parameter $\boldsymbol{\alpha}_\mathrm{i}$, given by $\underline{\mathbf{x}_\mathrm{i}}$ = [0.8, 0.35, 0.5, 0.25, 7, 0.3, 0.2, 0.2] $\overline{\mathbf{x}_\mathrm{i}}$ = [3, 3, 3, 1, 13.5, 1, 1, 1.5].

2.2 Deep Neural Network-based inverse design strategy

In a standard approach, the effective properties of numerous designs during the iterative optimization process are evaluated using the computational homogenization method (Fig. 2a). Such an iterative approach deems to be computationally expensive if many unit cells need to be designed for a large-scale heterogenous lattice structure. To this end, a back-propagation neural network (BPNN) that serves as a surrogate model is proposed to significantly improve the design efficiency for the following superiorities:

- Compared with the computational homogenization approach, the BPNN can predict the effective properties almost instantaneously, which reduces computing time significantly.
- Design sensitivity analysis based on computational homogenization is complicated and the accuracy may be affected by the perturbation rate if a non-analytical method is used, while for the BPNN, the sensitivity analysis can be concisely, quickly, and easily calculated using an explicit analytical function.

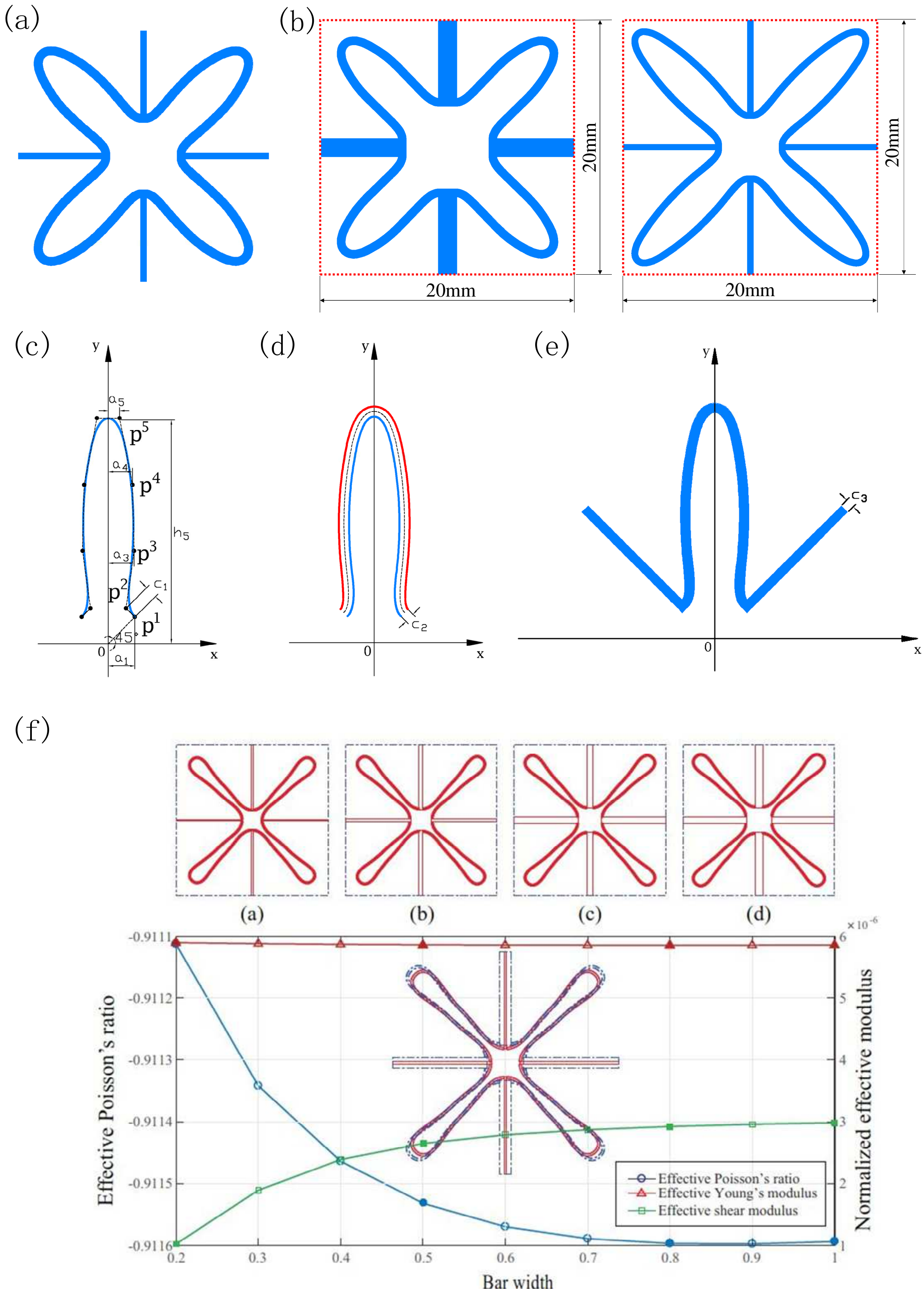

Figure 1. (a)Tetra-petal unit cell. (b) Outer size of tetra-petal unit cells. (c) The inner boundary of a tetra-petal unit cell and its dimension definition. (d) The inner and outer boundary of a tetra-petal unit cell. (e) Connecting bars' generation and width. (f) Influence of bar width on effective elastic properties [34].

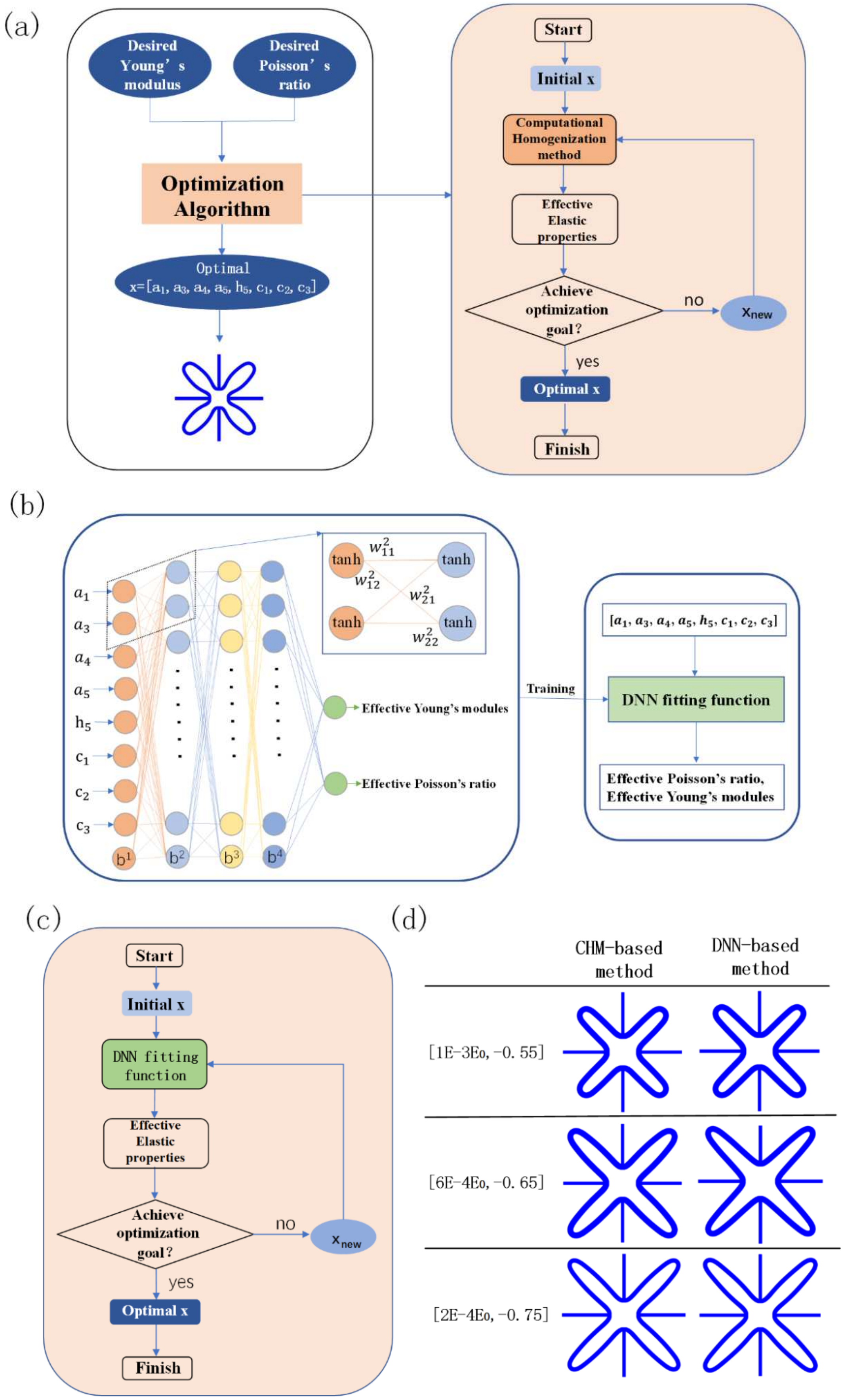

Figure 2. (a) Optimization method of tetra-petal unit cell design based on

computational homogenization method. (b) DNN structure. (c) Optimization method of tetra-petal unit cell design based on DNN fitting function. (d) Three tetra-petal unit cells generated using optimization methods based on the computational homogenization method (left) and the DNN approach.

Training a BPNN in the present context is a regression that establishes a mapping between the geometric design parameters as inputs and the effective properties as outputs. To ensure the accuracy of the surrogate model, a deep neural network (DNN) with two or more hidden layers can be utilized. The current framework consists of an input layer with eight neurons corresponding to 8 input design parameters that describe tetra-petal geometry, three hidden layers, and one output layer with two neurons predicting the effective Poisson's ratio and Young's modulus, as shown in Fig. 2b. The DNN can be used to replace the computational homogenization method for predicting effective properties for a new design parametrization during the inverse design of tetra-petal auxetics (Fig. 2c). A detailed account of such a DNN can be found in the work of Liao et. al. [48]. The DNN datasets of the training, validation, and test are 8050, 3450, and 500, respectively. The relative error (absolute value) distributions of the two effective property indexes for the test set are plotted in Fig 3. The relative error of the effective Poisson's ratios for some samples is large because the actual effective Poisson's ratio is close to zero.

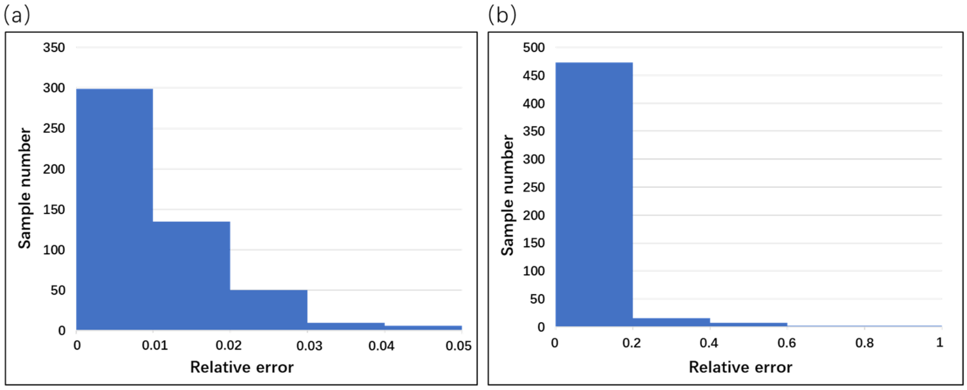

Figure 3. (a) The relative error (absolute value) distribution of the effective Young's modulus. (b) The relative error (absolute value) distribution of the effective Poisson's ratio.

Next, three tetra-petal design cases with different target properties were considered to compare the computational efficiency of the design optimization using computational homogenization and DNN-based approaches. The target Young's modulus and Poisson's ratio for the three cases are set as [1E-3E$_0$, -0.55], [6E-4E$_0$, -0.65], and [2E-4E$_0$, -0.75], respectively, where E$_0$ is the base material Young's modulus. The designed tetra-petals are shown in Fig. 2d. The accuracy and performance of these design approaches are compared in Table 1. The DNN-based approach significantly reduced the design optimization cost as compared to the computational homogenization-based approach.

Table 1 Comparison of computational homogenization-based and DNN-based methods.

	CHM-based method			DNN-based method		
	Time	Effective	Effective	Time [s]	Effective	Effective

	[s]	Young's modulus	Poisson's ratio		Young's modulus	Poisson's ratio
[1E-3E_0, -0.55]	773.60	1.00E-3 E_0	-0.55	7.92	1.00E-3 E_0	-0.56
[6E-4E_0, -0.65]	532.67	6.00E-4 E_0	-0.65	4.81	5.98E-4 E_0	-0.66
[2E-4E_0, -0.75]	573.05	2.00E-4 E_0	-0.75	4.89	1.97E-4 E_0	-0.76

3. Design and fabrication of functionally graded tetra-petal auxetic lattices

3.1 DNN-enhanced design framework for functionally graded tetra-petal auxetic lattices

Functionally graded lattices can be designed to provide a trade-off between structural and functional performance while ensuring light-weighting. In this study, the impact performance of functionally graded tetra-petal auxetics is investigated. To design such lattices, unit cells at different locations need to be tailored individually or in groups and the inverse design of each unit cell can be costly using traditional computational homogenization-based approach. Here, a lattice structure with three layers of grading with the same tetra-petal design throughout a given layer is adopted. A DNN-based inverse design approach is utilized for rapidly designing the graded auxetic lattices. The design domain of the lattice structure is a rectangular region with a dimension of $60\text{mm} \times 62\text{mm}$, with the top and bottom layer having a thickness of 1mm.

Lattice structures with overall dimensions of $60\text{mm} \times 62\text{mm}$ are inversely designed using the DNN-based design optimization approach. First, two graded auxetic lattices were obtained with effective Poisson's ratios of -0.7 and -0.5, respectively. The three graded layers are designed to have an effective Young's moduli of approximately 1.0E-04 E_0, 3.0E-04 E_0 and 9.0E-04 E_0, respectively. Next, three standard uniform lattices are obtained with an effective Poisson's ratio of -0.7 and different effective Young's moduli of approximately 1.0E-04 E_0, 3.0E-04 E_0 and 9.0E-04 E_0. The actual elastic properties of the tetra-petal auxetic unit cells calculated by the computational homogenization approach are summarized in Table 2. The geometries of tetra-petal unit cells are shown in Fig. 4d.

Table 2 The actual elastic properties of the designed tetra-petal unit cells calculated by the computational homogenization method.

	Effective Young's modulus	Effective Poisson's ratio
U7_1	1.01E-04 E_0	-0.691
U7_3	3.00E-04 E_0	-0.694
U7_9_1	8.94E-04 E_0	-0.719
U7_9_2	8.93E-04 E_0	-0.703
U5_1	1.02E-04 E_0	-0.491
U5_3	3.03E-04 E_0	-0.493
U5_9	8.99E-04 E_0	-0.495

Inversely designed tetra-petal unit cells and the construction of all the digital models were performed with a desktop computer, Y900 341SZ, with a CPU of the Intel(R) Core (TM) i7-6700K CPU @ 4.00GHz. The RAM is 16GB. The GPU is

NVIDIA GeForce GTX 1080. All uniform and graded tetra-petal digital models are constructed using Rhino 6. Two thin plates were added to the top and bottom of the lattice models for stabilizing the lattice surface during the impact tests, as shown in Fig. 4b.

The graded lattices can be oriented in two different ways during the impact testing, either the softer layer to be placed upwards or downwards. In this study, a graded auxetic lattice structure with the Poisson's ratio of -0.7 and an increasing or decreasing stiffness is labelled as 7_139 or 7_931, respectively (refer Fig. 4a). Similarly, the graded lattice structure with a Poisson's ratio of -0.5 is labelled as 5_139 or 5_931 depending upon the soft layer placed either upward or downward, respectively (refer Fig. 4a). The uniform auxetic lattices with different effective Young's modulus of 1.0E-04 E_0, 3.0E-04 E_0 and 9.0E-04 E_0 are referred as 7_111, 7_333, and 7_999_1 (refer Fig.4c), hereinafter. It should be noted that all three lattice structures with uniform cells have the same-sized thin connecting bars, and inevitably, the stability under impact decreases significantly as the unit stiffness increases. To ensure stability, an extra auxetic lattice for the petal unit with larger-sized connecting bars but the same moduli of 9.0E-04 E_0 is fabricated, termed 7_999_2 hereinafter, and the corresponding unit cell is termed U7_9_2.

3.2 **Additive manufacturing of auxetic lattices**

The generated uniform and graded auxetic lattice structures with a thickness of

60mm were fabricated with Flexible 80A resin in a Form 2 3D printer (Formlabs Inc., Boston USA) using stereolithography. The material properties of the resin are listed in Table 3. The geometric models were sliced using PreForm 3.23.1 software. All printed samples were washed in ethanol 75% (Fu Yu Fine Chemicals Ltd. - Tianjin, China) to remove residual liquid resin and cured under the sun light before the support removal. The 3D-printed tetra-petal auxetic structures are illustrated in Fig. 4e.

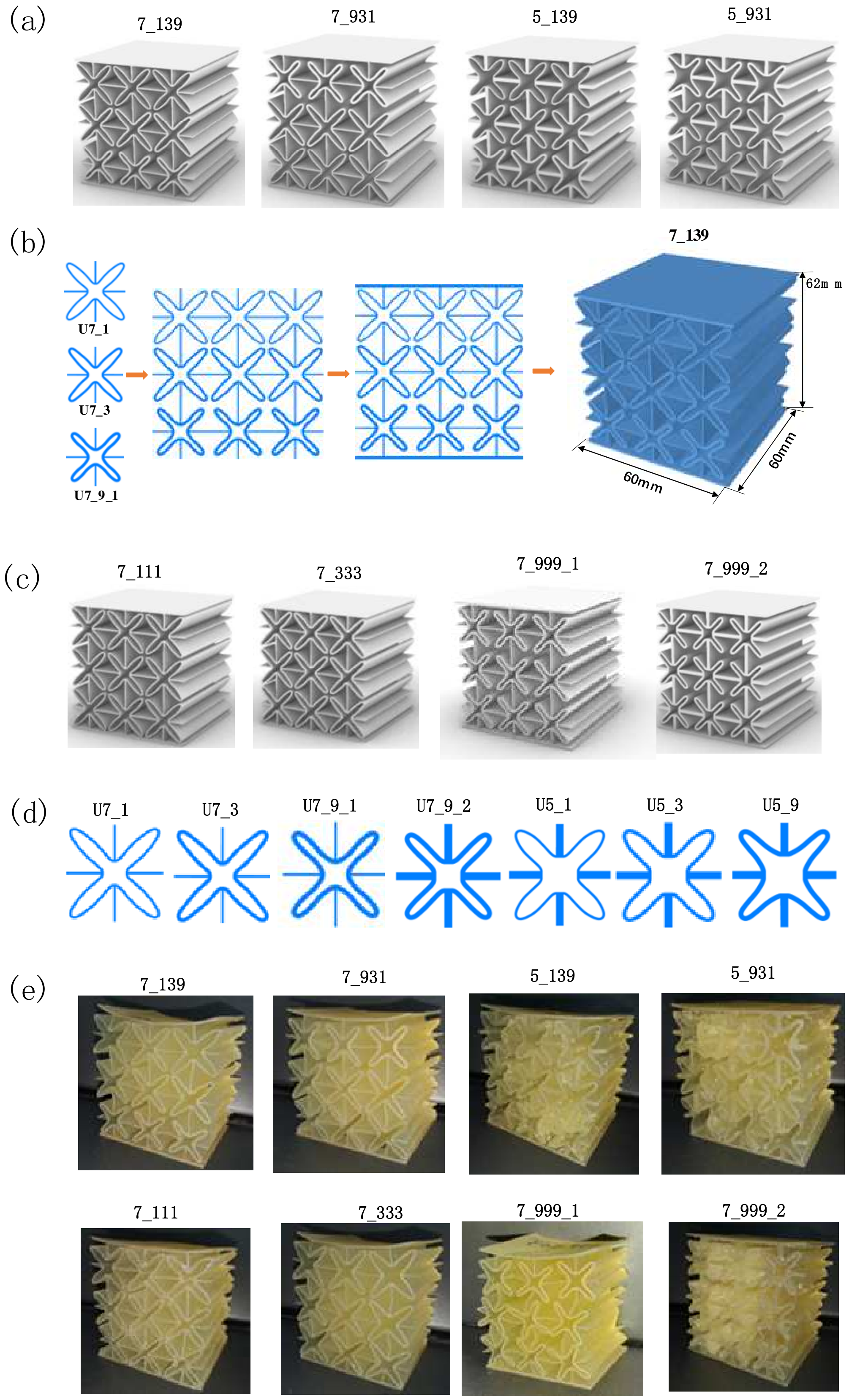

Figure 4. (a) Four graded auxetic lattices. (b) Model construction process. (c) Four non-graded auxetic lattices. (d) Tetra-petal unit cells. (e) 3D- printed samples. The

first number, 7, in U7_1, U7_3…, and 7_139,7_931 represents the unit cells with an effective Poisson's ratio of approximately -0.7. The second number in U7_1, U7_3…, represents the relative Young's modulus. For example, U7_1 represents the unit cell with an effective Poisson's ratio of approximately -0.7 and a Young's modulus of approximately 1.0E-04E_0, while U7_3 represents the unit cell with an effective Poisson's ratio of approximately -0.7 and a Young's modulus of approximately 3.0E-04E_0. The numbers after the underscore in 7_139,7_931… denote the construction of the auxetic lattice setting. For example, 7_139 represents the auxetic lattice formed by unit cells of U7_1 in the top layer, U7_3 in the middle layer, and U7_9 in the bottom layer, respectively; while U7_931 means the auxetic lattice formed by unit cells of U7_9 in the top layer, U7_3 in the middle layer, and U7_9 in the bottom layer, respectively.

Table 3 Resin material properties[58].

	Green	Post-cured
Ultimate tensile strength	3.7 MPa	8.9 MPa
Stress at 50% Elongation	1.5 MPa	3.1 MPa
Stress at 100% Elongation	3.5 MPa	6.3 MPa
Elongation at Break	100%	120%
Tear Strength	11 kN/m	24 kN/m

4. Impact tests of functionally graded tetra-petal auxetic lattices

4.1 Impact test setting

Impact tests are performed on the functionally graded auxetic lattice samples by placing them on a platform as shown in Fig. 5a. The platform consists of a support column, a support arm, a hollow cylindrical guide rail, a height adjuster, an impact pedestal, and an impact rod. Before commencing experiments, the hollow cylindrical guide rail is set to be vertical with ground to make sure that the impact rod falls smoothly, and the friction effect is minimized. The samples are aligned along the hollow cylindrical guide rail such that the impact rod falls on the centers of the samples. In a test, the impact rod is lifted to a certain level and released so that it falls onto the samples and the reaction force is measured by an acceleration sensor (Fig. 5b) simultaneously. To ensure the measurement precision and protect the sensor from damage during the test, the acceleration sensor is glued to a dice firmly and the assembly and disassembly of the impact rod are acted on the dice rather than directly on the sensor (Fig. 5c). The arrow engraved on the sensor represents its positive direction. The measured acceleration is negative when it is pointing upward.

4.2 Results

Impact tests for all samples are performed with the impact rod released from 5cm, 10cm, and 15cm above the top of the samples (Fig. 5d). To ensure that sensor collects the whole impact process data, the impact rod is released after the sensor is triggered. Each impact test is repeated five times to reduce the experimental error. The acceleration sensor outputs acceleration-time graphs and the peak acceleration magnitudes are recorded. For each tetra-petal sample, the datasets from five experimental repetitions with the same release height are acquired. The datasets with the minimum and the maximum peak acceleration speed are removed, and the rest three data sets are retained, as depicted in Table 4. The averages of all peak acceleration rates are compared in Fig. 6. It should be noted that the maximum acceleration magnitudes of the uniform sample 7_999_2 at 15cm are out of the acceleration sensor range (± 490 m/s²)[59] and hence the data collected for this testing case are not reliable, which is marked with underlines.

Table 4 Three retained maximum acceleration magnitudes and the averages of these quantities for all test samples at three different rod-releasing heights.

	5cm				10cm				15cm			
	Three maximum acceleration magnitudes [m/s^2]			AVG [m/s^2]	Three maximum acceleration magnitudes [m/s^2]			AVG [m/s^2]	Three maximum acceleration magnitudes [m/s^2]			AVG [m/s^2]
7_111	111.15	112.20	112.52	111.96	171.43	172.67	174.27	172.79	209.66	210.85	215.33	211.95
7_333	115.45	116.96	117.60	116.67	194.41	198.17	201.97	198.18	240.42	242.43	251.22	244.69
7_999_2	288.99	289.22	292.83	290.35	478.23	481.70	483.31	481.08	604.02	609.60	610.75	608.12
7_139	95.86	99.38	99.88	98.37	143.51	146.12	150.05	146.56	182.51	190.02	194.14	188.89
7_931	104.64	106.06	106.89	105.86	153.49	156.23	162.78	157.5	185.81	195.05	204.12	194.99
5_139	123.18	124.05	127.94	125.06	183.33	188.69	188.83	186.95	260.15	269.81	272.69	267.55
5_931	122.18	124.28	124.88	123.78	184.02	184.48	186.26	184.92	253.83	254.15	255.62	254.53

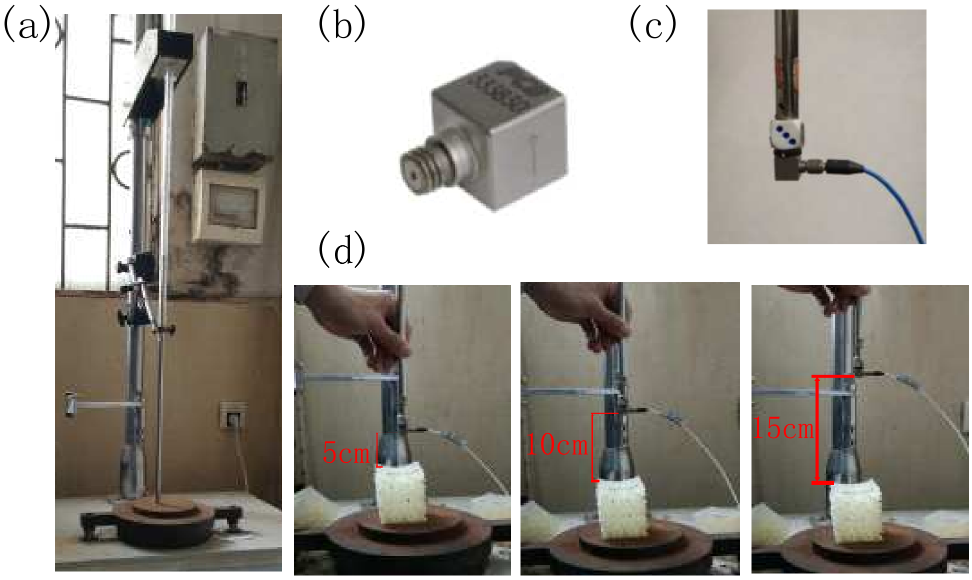

Figure 5. (a) Impact test platform. (b) Acceleration sensor. (c) Attachment of the acceleration sensor and the impact rod. (d) The impact rod is released from a height of 5cm, 10cm, and 15cm, respectively.

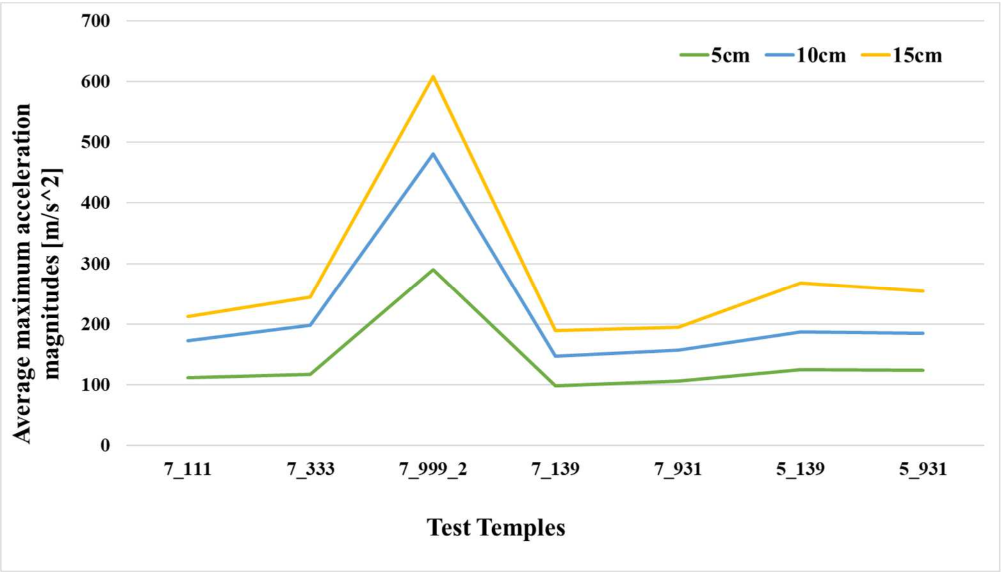

Figure 6. The average maximum acceleration magnitudes of all test samples with different levels of impact energy.

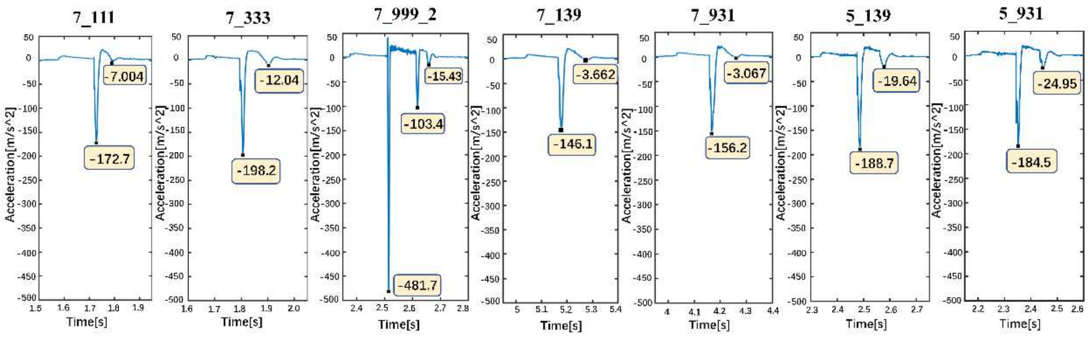

Figure 7. Acceleration curves of all test samples for the cases where the impact rod is released at a height of 10cm.

As shown in Fig 6, for every tetra-petal sample, the higher the impact energy is, the larger the average peak acceleration rate is. The differences between the average maximum acceleration magnitudes of samples 7_139 and 7_931 are 7.61% at 5cm, 7.46% at 10cm, and 3.23% at 15cm. Lattice sample 7_139 performs better than sample 7_931 for all three impact settings. Compared with sample 7_111 with uniform cells U7_1, graded sample 7_931 reduces the maximum acceleration magnitude by 5.45% at 5cm, 8.85% at 10cm, and 8.00% at 15cm. Compared with sample 7_333 with uniform cells U7_3, graded sample 7_931 reduces the average maximum acceleration magnitudes by 9.27% at 5cm, 20.53% at 10cm, and 20.31% at 15cm. Compared with sample 7_999_2 with uniform cells U7_9_2, graded sample 7_931 reduces the average maximum acceleration magnitudes by 63.54% at 5cm, 67.26% at 10cm, and 67.94% at 15cm. In summary, graded samples 7_139 and 7_931 perform better than uniform cell samples 7_111, 7_333, and 7_999_2. The differences between the average maximum acceleration magnitudes of graded samples 5_139 and 5_931 are -1.02% at 5cm, -1.09% at 10cm, and -4.87% at 15cm. Graded sample

5_931 has a slightly better performance at all three impact heights than sample 5_931. Compared with sample 5_931, sample 7_931 reduces the average maximum acceleration magnitudes by 14.48% at 5cm, 14.83% at 10cm, and 23.39% at 15cm. Graded samples 7_139 and 7_931 reduce the maximum acceleration magnitude more significantly than samples 5_139 and 5_931, indicating graded tetra-petals auxetic lattices with a Poisson's ratio of -0.7 have better performance than those with a Poisson's ratio of -0.5.

Selected acceleration-time graphs with a rod dropping height of 10 cm are depicted in Fig. 7. As shown in the graphs, all acceleration graphs show almost the same change trend along the time axis. The peak acceleration rates are negative, indicating that the resistance load from the samples to the impact rod is pointing upward. All graphs have only two upward acceleration peak values and the second peak value is prominently smaller than the first one, except the uniform sample 7_999_2 which has three peak values. For all cases, the second acceleration peak values reduce by 95.94% (uniform sample 7_111), 93.93% (uniform sample 7_333), 78.53% (uniform sample 7_999_2), 97.49% (graded sample 7_139), 98.04% (graded sample 7_931), 89.59% (graded sample 5_139), and 86.48% (graded sample 5_931), respectively, compared with the first acceleration peak values. This indicates that the impact rod does not have any obvious bounce after contacting with the samples.

5. Conclusion

The DNN trained to map the relation between geometry parameters of tetra-petal units and their effective elastic properties significantly improves the inverse design efficiency, compared with the traditional design approach using computational homogenization. This is favorable for functionally graded lattices where inverse tailor design is required locally for many unit cells. Leveraging such an efficient inverse design framework using DNN, we propose to design functionally graded tetra-petal auxetic lattices using the DNN-based inverse approach, with remarkable effectiveness and efficiency. Additive manufacturing technology is utilized to prototype the functionally graded and non-graded samples. Impact tests are performed over different designs and the results show promising performances. The improved impact resistance of graded auxetic lattice structures proves the feasibility of the proposed inverse design framework for functionally graded tetra-petal auxetic, which can be inspirable and helpful to promote advanced functional materials and structures with tunable behaviors.

Appendix

Table A1 The geometric parameters of tetra-petal unit cells.

Tetra-petals	α							
U7_1	1.41	1.37	1.28	0.60	11.95	0.66	0.54	0.50
U7_3	1.36	1.24	0.96	0.61	11.72	0.64	0.77	0.50
U7_9_1	1.27	0.39	0.70	0.45	10.05	0.70	0.96	0.50

U7_9_2	1.11	0.62	0.70	0.46	9.34	0.73	0.92	1.50
U5_1	1.86	1.56	1.59	0.62	10.61	0.64	0.48	1.50
U5_3	1.77	1.36	1.39	0.62	10.12	0.66	0.67	1.50
U5_9	2.00	0.96	0.85	0.48	9.97	0.53	0.94	1.50

Acknowledgements

This work is supported by National Natural Science Foundation of China [No. 52075184] (J. Li, Y. Wang). This research is supported by A*STAR <C210112026> (Z. P. Wang). Portions of the research were supported by the U.S. Department of Energy, Office of Energy Efficiency and Renewable Energy, Industrial Technologies Program, under contract DE-AC05–00OR22725 with UT Battelle, LLC.

References

[1] Wessel JK. The handbook of advanced materials: enabling new designs: John Wiley & Sons; 2004.

[2] Nemat-Alla M. Reduction of thermal stresses by developing two-dimensional functionally graded materials. International journal of solids and structures. 2003;40:7339-56.

[3] Choi KH, Kim H-S, Park CH, Kim G-H, Baik KH, Lee SH et al. High-temperature thermo-mechanical behavior of functionally graded materials produced by plasma sprayed coating: Experimental and modeling results. Metals and Materials International. 2016;22:817-24.

[4] Bahrami S, Ovesy HR, Shakeri M. Dynamic analysis of functionally graded circular cylindrical panel with piezoelectric fiber composite actuator and sensor. Journal of Intelligent Material Systems and Structures. 2015;26:2369-85.

[5] Atashipour S, Sburlati R. Electro-elastic analysis of a coated spherical piezoceramic sensor. Composite Structures. 2016;156:399-409.

[6] Mehrali M, Shirazi FS, Mehrali M, Metselaar HSC, Kadri NAB, Osman NAA. Dental implants from functionally graded materials. Journal of Biomedical Materials Research Part A: An Official Journal of The Society for Biomaterials, The Japanese Society for Biomaterials, and The Australian Society for Biomaterials and the Korean Society for Biomaterials. 2013;101:3046-57.

[7] Lowen JM, Leach JK. Functionally graded biomaterials for use as model systems and replacement tissues. Advanced Functional Materials. 2020;30:1909089.

[8] Zhu C, Qiu J, Thomopoulos S, Xia Y. Augmenting Tendon‐to‐Bone Repair with Functionally Graded Scaffolds. Advanced Healthcare Materials. 2021;10:2002269.

[9] Zhang Y, Malyi OI, Tang Y, Wei J, Zhu Z, Xia H et al. Reducing the charge carrier transport barrier in functionally layer‐graded electrodes. Angewandte Chemie. 2017;129:15043-8.

[10] Rasel S, Bhatkar O, Smith D, Kowal MD, Anderson M, Rizvi R et al. Self-assembled functionally graded graphene films with tunable compositions and their applications in transient electronics and actuation. ACS applied materials & interfaces. 2019;11:23463-73.

[11] Xu F, Zhang X, Zhang H. A review on functionally graded structures and materials for energy absorption. Engineering Structures. 2018;171:309-25.

[12] Baroutaji A, Arjunan A, Stanford M, Robinson J, Olabi AG. Deformation and energy absorption of additively manufactured functionally graded thickness thin-walled circular tubes under lateral crushing. Engineering Structures. 2021;226:111324.

[13] NTopology. Architected Materials. [cited 2023 January 8th]; Available from: https://ntopology.com/architected-materials/.

[14] Altair. Altair OptiStruct® Revolutionizes Lattice Structures for 3D Printing. [cited 2023 January 8th]; Available from: http://www.altairhyperworks.com/newsdetail.aspx?news_id=11109&news_country=en-US

[15] Materialise. Materialise 3-matic Lightweight Structures Module. [cited 2023 January 8th]; Available from: http://www.materialise.com/en/software/3-matic/modules/lightweight-structures-module

[16] Dirrenberger J, Forest S, Jeulin D. Effective elastic properties of auxetic microstructures: anisotropy and structural applications. International Journal of Mechanics and Materials in Design. 2013;9:21-33.

[17] Alderson KL, Fitzgerald A, Evans KE. The strain dependent indentation resilience of auxetic microporous polyethylene. Journal of Materials Science. 2000;35:4039-47.

[18] Zhu Y, Wang Z-P, Poh LH. Auxetic hexachiral structures with wavy ligaments for large elasto-plastic deformation. Smart Materials and Structures. 2018;27:055001.

[19] Zhu Y, Zeng Z, Wang Z-P, Poh LH, Shao Y. Hierarchical hexachiral auxetics for large elasto-plastic deformation. Materials Research Express. 2019;6:085701.

[20] Zhao X, Wei L, Wen D, Zhu G, Yu Q, Ma Z. Bending response and energy absorption of sandwich beams with novel auxetic honeycomb core. Engineering Structures. 2021;247:113204.

[21] Spadoni A, Ruzzene M, Gonella S, Scarpa F. Phononic properties of hexagonal chiral lattices. Wave motion. 2009;46:435-50.

[22] Yeganeh-Haeri A, Weidner DJ, Parise JB. Elasticity of α-cristobalite: a silicon dioxide with a negative Poisson's ratio. Science. 1992;257:650-2.

[23] Keskar NR, Chelikowsky JR. Negative Poisson ratios in crystalline SiO2 from first-principles calculations. Nature. 1992;358:222-4.

[24] Theocaris P, Stavroulakis G, Panagiotopoulos P. Negative Poisson's ratios in composites with star-shaped inclusions: a numerical homogenization approach. Archive of Applied Mechanics. 1997;67:274-86.

[25] Masters I, Evans K. Models for the elastic deformation of honeycombs. Composite structures. 1996;35:403-22.

[26] Smith CW, Grima J, Evans K. A novel mechanism for generating auxetic behaviour in reticulated foams: missing rib foam model. Acta materialia. 2000;48:4349-56.

[27] Zhu Y, Luo Y, Gao D, Yu C, Ren X, Zhang C. In-plane elastic properties of a novel re-entrant auxetic honeycomb with zigzag inclined ligaments. Engineering Structures. 2022;268:114788.

[28] Prall D, Lakes R. Properties of a chiral honeycomb with a Poisson's ratio of—1. International Journal of Mechanical Sciences. 1997;39:305-14.

[29] Spadoni A, Ruzzene M. Elasto-static micropolar behavior of a chiral auxetic lattice. Journal of the Mechanics and Physics of Solids. 2012;60:156-71.

[30] Grima JN, Evans KE. Auxetic behavior from rotating triangles. Journal of materials science. 2006;41:3193-6.

[31] Grima JN, Evans KE. Auxetic behavior from rotating squares. Journal of Materials Science Letters. 2000;19:1563-5.

[32] Wang Z-P, Poh LH, Dirrenberger J, Zhu Y, Forest S. Isogeometric shape optimization of smoothed petal auxetic structures via computational periodic homogenization. Computer Methods in Applied Mechanics and Engineering. 2017;323:250-71.

[33] Wang Z-P, Poh LH. Optimal form and size characterization of planar isotropic petal-shaped auxetics with tunable effective properties using IGA. Composite Structures. 2018;201:486-502.

[34] Wang Z-P, Poh LH, Zhu Y, Dirrenberger J, Forest S. Systematic design of tetra-petals auxetic structures with stiffness constraint. Materials & Design. 2019;170:107669.

[35] Pokkalla DK, Poh LH, Quek ST. Isogeometric shape optimization of missing rib auxetics with prescribed negative Poisson' s ratio over large strains using genetic algorithm. International Journal of Mechanical Sciences. 2021;193:106169.

[36] Pokkalla DK, Wang Z, Teoh JC, Poh LH, Lim CT, Quek ST. Soft Missing Rib Structures with Controllable Negative Poisson' s Ratios over Large Strains via Isogeometric Design Optimization. Journal of Engineering Mechanics. 2022;148:04022063.

[37] Qiao J, Chen C. Impact resistance of uniform and functionally graded auxetic double arrowhead honeycombs. International Journal of Impact Engineering. 2015;83:47-58.

[38] Novak N, Borovinšek M, Vesenjak M, Wormser M, Körner C, Tanaka S et al. Crushing behavior of graded auxetic structures built from inverted tetrapods under impact. physica status solidi (b). 2019;256:1800040.

[39] Xiao D, Dong Z, Li Y, Wu W, Fang D. Compression behavior of the graded metallic auxetic reentrant honeycomb: Experiment and finite element analysis. Materials Science and Engineering: A. 2019;758:163-71.

[40] Zhao S, Zhang Y, Wu H, Zhang Y, Yang J, Kitipornchai S. Tunable nonlinear bending behaviors of functionally graded graphene origami enabled auxetic metamaterial beams. Composite Structures. 2022;301:116222.

[41] Zhao S, Zhang Y, Zhang Y, Yang J, Kitipornchai S. Vibrational characteristics of functionally graded graphene origami-enabled auxetic metamaterial beams based on machine learning assisted models. Aerospace Science and Technology. 2022;130:107906.

[42] Zhao S, Zhang Y, Wu H, Zhang Y, Yang J. Functionally graded graphene origami-enabled auxetic metamaterial beams with tunable buckling and postbuckling resistance. Engineering Structures. 2022;268:114763.

[43] Zhao S, Zhang Y, Zhang Y, Yang J, Kitipornchai S. A functionally graded auxetic metamaterial beam with tunable nonlinear free vibration characteristics via graphene origami. Thin-Walled Structures. 2022;181:109997.

[44] Akbar, A., Javadi, Asaad, Faramarzi, Raziyeh et al. Design and optimization of microstructure of auxetic materials. Engineering Computations. 2012;29:260-76.

[45] Clausen A, Wang F, Jensen JS, Sigmund O, Lewis JA. Topology optimized architectures with programmable Poisson’ s ratio over large deformations. Adv Mater. 2015;27:5523-7.

[46] Pokkalla DK, Wang Z-P, Poh LH, Quek ST. Isogeometric shape optimization of smoothed petal auxetics with prescribed nonlinear deformation. Computer Methods in Applied Mechanics and Engineering. 2019;356:16-43.

[47] Zhu Y, Jiang S, Li J, Pokkalla DK, Wang Q, Zhang C. Novel isotropic anti-tri-missing rib auxetics with prescribed in-plane mechanical properties over large deformations. International Journal of Applied Mechanics. 2021;13:2150115.

[48] Liao Z, Wang Y, Gao L, Wang Z-P. Deep-learning-based isogeometric inverse design for tetra-chiral auxetics. Composite Structures. 2022;280:114808.

[49] Wang Y, Liao Z, Shi S, Wang Z, Poh LH. Data-Driven Structural Design Optimization for Petal-Shaped Auxetics Using Isogeometric Analysis. Computer Modeling in Engineering & Sciences. 2020:122.

[50] Hou Y, Neville R, Scarpa F, Remillat C, Gu B, Ruzzene M. Graded conventional-auxetic Kirigami sandwich structures: Flatwise compression and edgewise loading. Composites Part B: Engineering. 2014;59:33-42.

[51] Hou W, Yang X, Zhang W, Xia Y. Design of energy-dissipating structure with functionally graded auxetic cellular material. International Journal of Crashworthiness. 2018;23:366-76.

[52] Qi D, Lu Q, He C, Li Y, Wu W, Xiao D. Impact energy absorption of functionally graded chiral honeycomb structures. Extreme Mechanics Letters. 2019;32:100568.

[53] Mahmoud D, Elbestawi MA. Lattice structures and functionally graded materials applications in additive manufacturing of orthopedic implants: a review. Journal of Manufacturing and Materials Processing. 2017;1:13.

[54] Maskery I, Aremu AO, Parry L, Wildman RD, Tuck CJ, Ashcroft IA. Effective design and simulation of surface-based lattice structures featuring volume fraction and cell type grading. Materials & Design. 2018;155:220-32.

[55] Plocher J, Panesar A. Effect of density and unit cell size grading on the stiffness and energy absorption of short fibre-reinforced functionally graded

lattice structures. Additive Manufacturing. 2020;33:101171.
[56] Li C, Shen H-S, Wang H. Nonlinear dynamic response of sandwich plates with functionally graded auxetic 3D lattice core. Nonlinear Dynamics. 2020;100:3235-52.
[57] Wu X, Su Y, Shi J. In-plane impact resistance enhancement with a graded cell-wall angle design for auxetic metamaterials. Composite Structures. 2020;247:112451.
[58] Formlabs. RESIN FAMILY-Flexible and Elastic. [cited 2022 May 13]; Available from: https://formlabs.com/materials/flexible-elastic/.
[59] PCB. Model : 333B30 | Accelerometer, ICP®. [cited 2022 May 13]; Available from: https://www.pcb.com/products?m=333b30.